Department of Precision and Microsystems Engineering

# Modelling Discrete Dislocation Dynamics with Discontinuity-Enriched Finite Element Analysis

Robbert-Jan Bosch


| | |
|---|---|
| Report no | : 2020.062 |
| Coaches | : C. Ayas, A. M. Aragón |
| Professor | : A. van Keulen, L. Nicola |
| Specialisation | : Structural Optimization and Mechanics |
| Type of report | : Thesis |
| Date | : 30 November 2020 |


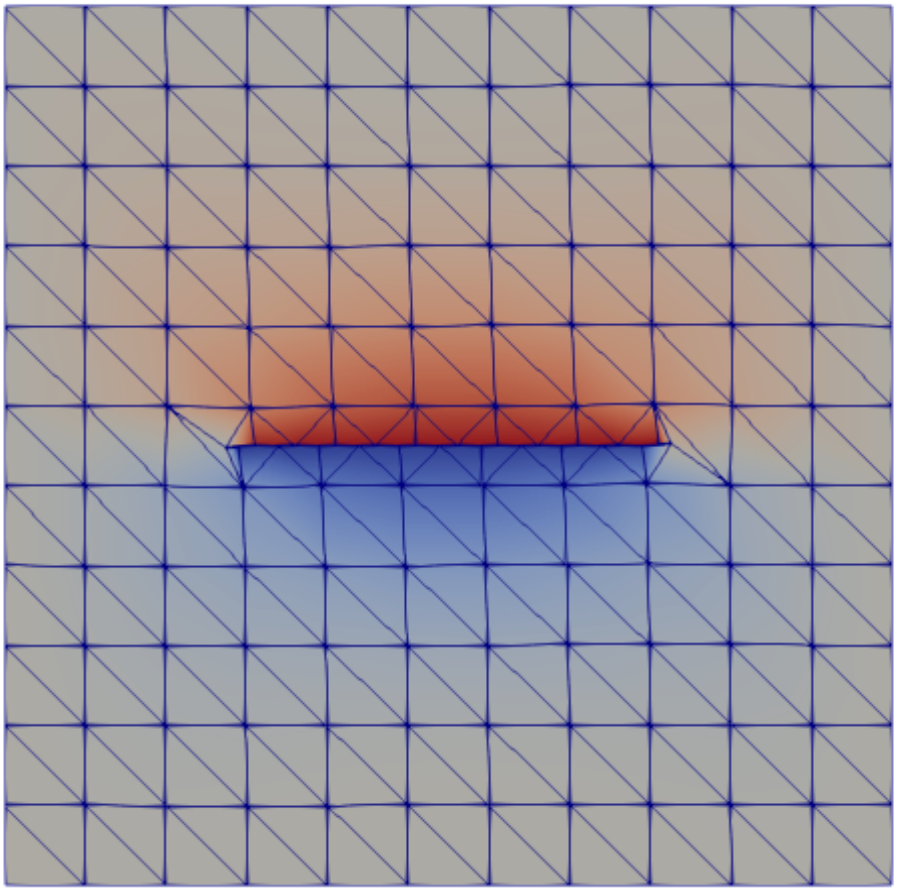

# ABSTRACT

Discrete Dislocation Dynamics concerns the analysis of microplasticity in which the dislocations, a line defect in the crystallographic periodicity, are treated as separate moving entities inside an elastic continuum. This analysis at the mesoscale can give valuable insights in the nature of dislocations and the behaviour of macroscopic plasticity. Although an analytical solution for dislocations exist, special measures are to be taken for the solution of boundary value problems. In this thesis a Discrete Dislocation Dynamic model in a two-dimensional plane-strain formulation for edge dislocations is proposed using DE-FEM, a finite element formulation enriched with discontinuities to model dislocations independent of the mesh. Although the modelling of a stationary field with dislocations is straightforward, the dynamic solution becomes much more complicated. It requires the accurate stress retrieval of the numerical stresses close to an artificial singularity and various attempts, such as eliminating the singularity by subtracting the analytical solution or incorporating a singular core enrichment, were proven to be ineffective. Recommendations are given for future attempts, but also an alternative numerical superposition approach is explained. Its results are comparable to existing methods in terms of accuracy, but the computation time is not optimal for the current implementation.

# Contents

# 1

# INTRODUCTION

Since the introduction of discrete dislocation (DD) simulations in 1992 [1], many DD simulation codes have emerged. By bridging the gap between molecular dynamics and continuum mechanics [2], discrete dislocation dynamics has proved a valuable tool to improve our understanding of microscale plasticity, but also for applications in strain hardening [3], nano-indentation [4] and tribology [5]. In order to simulate simple geometries and account for boundary conditions, the general approach is to compute the infinite domain analytical stress field for each dislocation, deduced by Hirth & Lothe [6], and superimpose them with an image stress field, obtained by FEM with "corrected" boundary conditions [7]. A limitation that remains is the $\mathcal{O}(n_d^2)$ dependency for computing the stress field for each of the $n_d$ dislocations. For actual problems with a large number of dislocations this can become a computational challenge. The basic implementation of the analytical solutions is in 2D, but for 3D discretization solutions exist, as well as Green's functions for some more complex geometries [8].

A generalized approach to incorporate discrete dislocations within the finite element method (FEM), and that lacks the latter limitations, was first pioneered by Ventura [9]. Based upon the partition-of-unity concept [10], it makes uses of the eXtended FEM or Generalized FEM [11, 12]), to incorporate *a priori* knowledge in the stress field and model arbitrary discontinuities, such as the presence of dislocations. This allows FEM to take both the stress fields of dislocations and the boundaries into account simultaneously. The concept was further developed for edge dislocations by Gracie [13], where a 2D dislocation was broken down into a glide plane and a core. The glide plane was modelled by a tangential Heaviside function and the core as the end of the plane, where a regularization was added to prevent infinite strains. To improve the overall accuracy, several more realistic core enrichments were proposed such as the analytical infinite domain solution [14–16], a combination with atomistic models [17] and the Peierls-Nabarro cutoff [18].

For the correct evaluation of these discontinuities in FEM, several approaches have been proposed for quadrature. A frequent occurring method is to split discontinuous elements up into subcells for integration [9, 13, 18, 19]. Another method to evaluate singularities is to transform the element domain integral into an equivalent contour integral [9, 14–16]. For the computation of the strain energy, the core is excluded from the calculation, because inside the core the strain energy is infinite [9, 13].

The driving force of dislocation dynamics is the Peach-Köhler force, which depends on the stress state around a dislocation, excluding the stress due to itself. This force is constantly updated as the field around the dislocation changes. Some form of superposition of stresses due to each of the dislocation is often used, such as using the analytical infinite domain solution as core enrichment and applying superposition locally [14], but alternatively it can also be computed with a small contour integral around the core [18, 20].

In the past decade there has not been much innovation in this field of dislocations with enriched FEM, apart from the use of higher order elements [18] and the application of aforementioned methods to single-walled carbon nanotubes [21], polycrystals [22], and crack simulation [23]. This thesis aims to further progress the computational models for discrete dislocation dynamics by modelling them with Discontinuity-Enriched FEM, a new enriched FE formulation [19].

The structure of this report is as follows. First a general background into discrete dislocation dynamics and enriched finite element analysis is given. The third chapter shows the modelling of a stationary dislo-

cation field using DE-FEM and demonstrates its accuracy in terms of displacement and stress. The fourth chapter is the simulation of moving dislocations over time using DE-FEM, and generally discusses two different approaches to do so, of which one is completely worked out and proven. The fifth and last chapter contains the conclusions and any remaining recommendations.

# 2

# BACKGROUND

In order to gain a full understanding of this work, the current context of dislocations, and available computational methods are explicated. What is a dislocation? What are its effects on a material? And what are the analytical ways of modelling a dislocation? That is discussed in the first section. The second section explains the numerical side of things. What computational methods are available for modelling dislocations? Its main focus is on explaining enriched finite element formulations, and its possible applications, such as modelling discrete dislocation dynamics.

## 2.1. DISLOCATIONS

A dislocation is a linear defect in the crystal structure of crystalline solids, e.g. metals, diamonds, rocks or ceramics [24] and a carrier of plasticity at the microscale. The presence of dislocations in large numbers strongly influences the properties of these materials. Hence an accurate description is required and the concept is shortly introduced here.

### 2.1.1. PLASTICITY

Plasticity, or plastic deformation, is the permanent deformation of a solid material. At the microscale it is primarily caused by two modes: slip and twinning. Slip is a shear deformation in which a plane of atoms moves with respect to another plane with a multiple distinct atomic spacings. The crystallographic orientation of the atoms at both sides of the slip plane is retained. For twinning there will be a reorientation across the twin plane and the atomic displacement is less than the interatomic separation. Both modes are shown in Figure 2.1. Slip is the prominent mechanism of plasticity. Macroscopic plastic deformation corresponds to the motion of large numbers of dislocations. The ability of a metal to deform plastically depends on the ability of dislocations to move inside. Therefore, a better understanding of the movement of discrete dislocations could greatly enhance our understanding of plasticity, especially in micro- or thin walled structures.

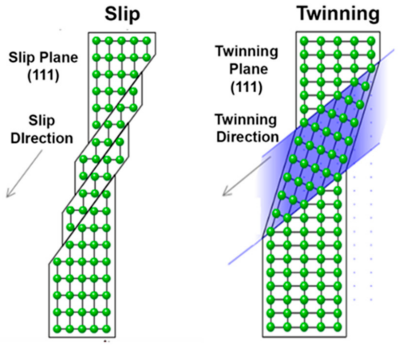


Figure 2.1: Image copied from Yang and Park, 2019 [25]. Slip and twinning in a face-centered cubic crystal. Slip occurs by gliding dislocations, causing crystal planes to slide along each other. Twinning reorders the atomic structure and mirrors it across the twinning plane.

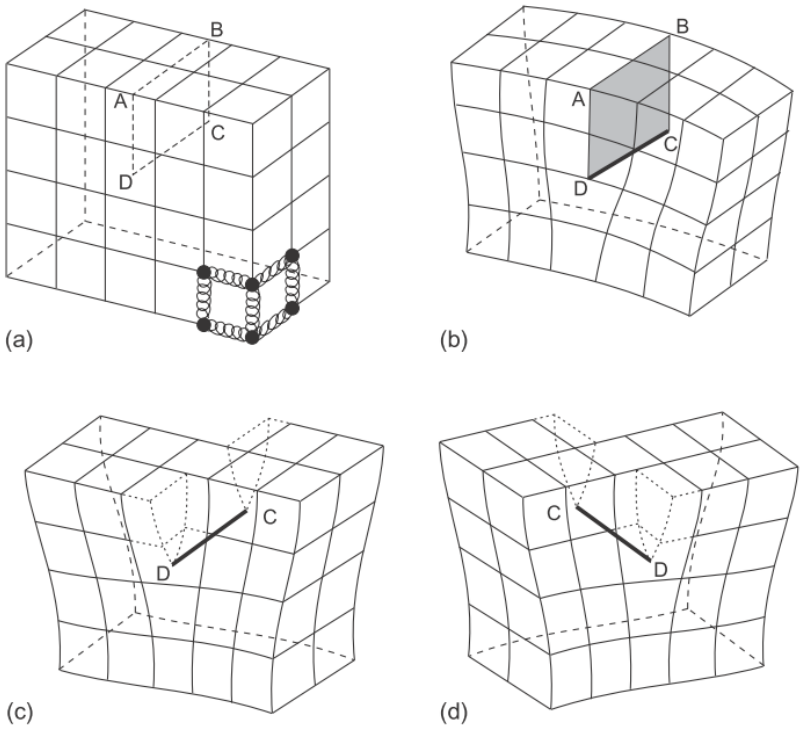


Figure 2.2: Image copied from Hull and Bacon, 2011 [24]. (a) Model of a simple cubic lattice; the atoms are represented by filled circles, and the bonds between atoms by springs, only a few of which are shown; (b) positive edge dislocation DC formed by inserting an extra half-plane of atoms in ABCD; (c) left-handed screw dislocation DC formed by displacing the faces ABCD relative to each other in direction AB; (d) right-handed screw dislocation DC

### 2.1.2. GEOMETRY

Zooming in on a single dislocation will reveal that it is an atomic line defect. It is a closed loop that separates an intact region from one where the lattice has undergone slip [24]. The relative shift between atomic planes is denoted by the Burgers vector $\boldsymbol{b}$ and it is unique for the entire dislocation. When the part of the loop is parallel with the slip direction, it is called the *screw* part of the dislocation. When its dislocation line is perpendicular with the slip, it is called the *edge* part of the dislocation. Each loop has at least two perfect edge, and two perfect screw dislocations. This is illustrated in Figure 2.2 [24].

It shows the simplified atomic arrangement for dislocations in a cubic structure. Figure 2.2(b) shows an extra plane of atoms inserted across the surface ABCD. A large disturbance is caused over line DC. This line is called a positive edge dislocation and denoted by $\perp$. A negative edge dislocation $\top$ is obtained when an extra plane of atoms is inserted below ABCD. A displacement or slip along the ABCD plane (parallel) is called a screw dislocation as in figure 2.2(c)(d). This disturbance due to the presence of a dislocation creates an internal source of stress.

#### BURGERS VECTOR AND BURGERS CIRCUIT

The geometry of a dislocation is governed by its slip plane, with unit normal vector $\boldsymbol{m}$, by the dislocation line with local tangent vector $\boldsymbol{t}$ and the Burgers vector $\boldsymbol{b}$. The Burgers vector is defined by making a circuit around a dislocation that would be closed in a perfect crystal. The vector required to close the loop in a dislocated crystal is the Burgers vector, as Figure 2.3(b) shows. Different conventions exist, but here the Start-Finish, right-hand rotation (SF/RH) convention is used as illustrated in the figure. The Burgers vector defines the relative shift of the atoms above the glide plane relative to those below it. In a planar model a dislocation loop can be modelled by a positive and a negative edge dislocation. Since they are parts of the same loop, they have the same Burgers vector. However, for a two dimensional atomic structure, the line direction $\boldsymbol{t}$, and therefore the circulation direction, is unknown. The convention for two-dimensional views here is that the Burgers circuit is always taken in the counter clockwise direction. In a continuum framework the definition

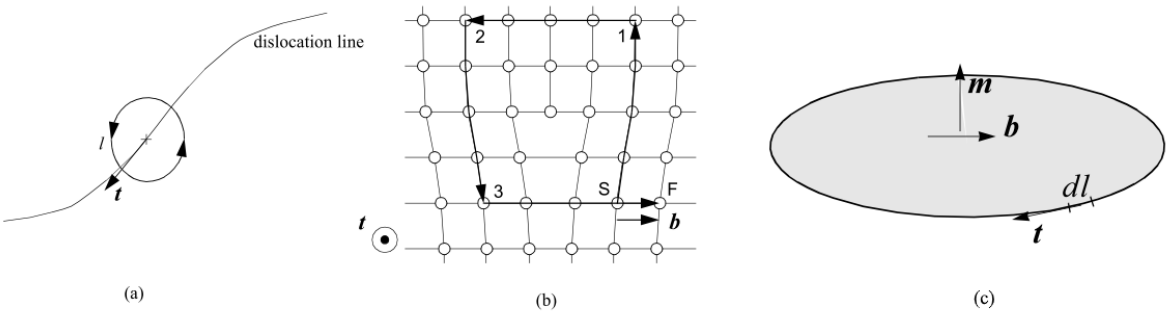


Figure 2.3: Burgers circuit. (a) General definition of circuit around a dislocation line in the right-handed sense (b) Right-handed circuit around an edge dislocation: the net vector from Start to Finish is the Burgers vector $\boldsymbol{b}$, according to SF/RH convention (c) Geometry of a dislocation loop, with slip plane unit normal vector $\boldsymbol{m}$

of the Burgers vector becomes the resultant of the contour integral

$$\boldsymbol{b} = \oint_C \frac{\partial \boldsymbol{u}}{\partial c} dc \tag{2.1}$$

where C is a closed circuit around the dislocation, c is the local traversing coordinate over C and $\boldsymbol{u}$ is the actual displacement field containing a dislocation. Note that for a perfect crystal, without a dislocation present, the resulting vector from start to finish is $\boldsymbol{b} = \boldsymbol{0}$. [24, 26]

### ANALYTICAL SOLUTION

For perfect edge or screw dislocations an analytical solution was obtained by Hirth and Lothe [6]. These are the relations for a dislocation inside an infinite elastic medium. Combining these two basis solutions allows modelling the entire dislocation loop. A screw dislocation can be modelled as anti-plane shear problem, where the only displacement is occurring out-of-plane:

$$u_1 = u_2 = 0 \tag{2.2}$$

$$u_3 = \frac{b}{2\pi} \arctan2(x_2, x_1) \tag{2.3}$$

And the only non-zero components of the stress tensor $\boldsymbol{\sigma}$ are $\sigma_{13}$ and $\sigma_{23}$, which are written in polar coordinates as

$$\sigma_{\theta z} = \frac{\mu b}{2\pi r} \tag{2.4}$$

An edge dislocation can be modelled as a plane strain problem. Inside an elastically isotropic material with shear modulus $\mu$ and Poisson's ratio $\nu$, and with a Burgers vector magnitude $b$ in $x$-direction, the resulting displacement field is

$$u_1 = \frac{b}{2\pi(1-\nu)} \left[ \frac{1}{2} \frac{x_1 x_2}{x_1^2 + x_2^2} - (1-\nu) \arctan\left(\frac{x_1}{x_2}\right) \right] \tag{2.5}$$

$$u_2 = \frac{b}{2\pi(1-\nu)} \left[ \frac{1}{2} \frac{x_2^2}{x_1^2 + x_2^2} - \frac{1}{4}(1-2\nu) \ln \frac{x_1^2 + x_2^2}{b^2} \right] \tag{2.6}$$

And the stress tensor $\boldsymbol{\sigma}$ for the posed plane strain configuration is

$$\boldsymbol{\sigma} = \begin{bmatrix} \sigma_{11} & \sigma_{12} & 0 \\ \sigma_{21} & \sigma_{22} & 0 \\ 0 & 0 & \sigma_{33} \end{bmatrix} \tag{2.7}$$

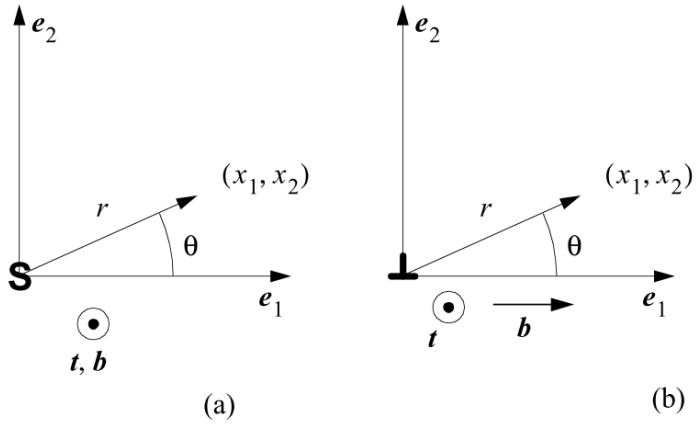


Figure 2.4: Analytical coordinate axes. (a) A screw dislocation, with an out-of-plane Burgers vector (b) An edge dislocation where the Burgers vector is in the plane.

with

$$\sigma_{11} = -\frac{\mu b}{2\pi(1-\nu)} \frac{x_2(3x_1^2 + x_2^2)}{(x_1^2 + x_2^2)^2} \tag{2.8}$$

$$\sigma_{22} = \frac{\mu b}{2\pi(1-\nu)} \frac{x_2(x_1^2 - x_2^2)}{(x_1^2 + x_2^2)^2} \tag{2.9}$$

$$\sigma_{12} = \sigma_{21} = -\frac{\mu b}{2\pi(1-\nu)} \frac{x_1(x_1^2 - x_2^2)}{(x_1^2 + x_2^2)^2} \tag{2.10}$$

It should be noted that for both the edge and the screw dislocation, the stresses are singular at the core, where $(x_1, x_2) = (0,0)$ or $r = 0$.

#### DISLOCATION STRUCTURES

At the mesoscale (~ 1 $\mu$m—200 $\mu$m) plastic deformation can be observed as the interaction of countless dislocations. Together they form certain structures. An effective analysis tool is to sum up all the Burgers vectors, yielding a net-Burgers vector over a certain area. A frequently occurring structure of dislocations is the dipole. In 2D models, a single dislocation loop can be characterised by a dipole, which comprises two dislocation cores with opposite Burgers vector of equal magnitude, and a connecting (straight) slip plane. Another relevant structure is a low-angle grain boundary, which is a wall of vertically stacked edge dislocations of the same sign. When a crystal is bent, there will be an excess of dislocations with the same sign, known as geometrically necessary dislocations. The energy of the crystal can be reduced by stacking the dislocations into a low-angle grain boundary. Because some regions mutually cancel, these boundaries have no long range stress field, but only influence a local region. Macroscale bending can also result from a random distribution of dislocations of the same Burgers vector, because it produces a misorientation of one edge relative to the other.

### 2.1.3. PLASTICITY MODELS

The modelling of plasticity can be evaluated by understanding the nature of dislocations at an atomic scale (~ nm ), or more zoomed out at a macroscopic scale, where the continuum principle holds (~ m), or somewhere in between. In Molecular Dynamics, atoms are the basic elements, and this model delineates a proper view of a single or a few dislocation lines. The simulation size however is limited to $<(200\,\text{nm})^3$, for a lack of computational power [2]. Dislocation Dynamics operate at the mesoscale (~ 1—200 µm), where dislocation lines are represented explicitly. The scale is large enough for the continuum principle to hold around the dislocations and each dislocation line is treated as an elastic inclusion embedded in an elastic medium. This model allows for simulation of dislocation interaction for a constrained volume of about $<(50\,\mu\text{m})^3$ [2]. In Continuum Plasticity individual dislocations are no longer modelled. Instead the plasticity behaviour follows from a set of constitutive rules based on experimental data and approximations. The differences in size and time are presented clearly in [2, Figure 2.5]. Due to a larger overlap between the models, more information

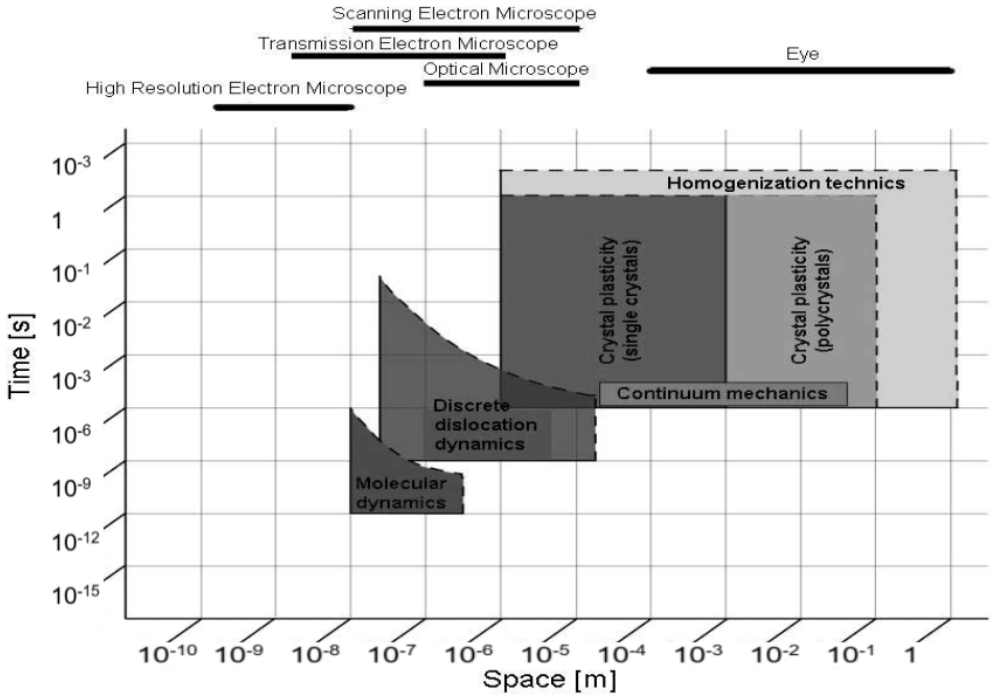


Figure 2.5: Image copied from Fivel, 2008 [2]. Typical volume size and physical time covered by three models devoted to crystal plasticity

can be exchanged which can improve the models further. This review focusses primarily on the simulations of Dislocation Dynamics, a powerful tool to model the behaviour of metallic materials at the mesoscale. Though there is some research in the field of Continuum Dislocation Dynamics [27], where the dislocation arrangements and kinematics are represented by continuous field variables, the main focus of this thesis will be *Discrete* Dislocation Dynamics. Treating the dislocations as separate (discrete) entities better illustrates the interaction between the individual dislocations and it gives a better approximation of the local stresses and failure points at given locations in the material.

### 2.1.4. DISLOCATION DYNAMICS

The study of dislocation dynamics gives an unique insight in the basic building blocks of plasticity at the mesoscale. Typical outputs of such simulations are firstly the dislocation structure and the stress field, but also global data such as dislocation density, the plastic slip and the stored energy. The motion of dislocations can be indexed in different types: glide, climb and cross-slip. Glide occurs when a dislocation moves within its slip plane. Climb is the motion of a dislocation orthogonal to its slip plane, and thus normal to the Burgers vector. For climb the dislocation has to move out of its slip plane, which requires the creation of a vacancy. Therefore climb motion is restricted to occur at higher temperatures and not considered here. Cross-slip is the phenomenon when a screw dislocation moves to another slip plane [24]. When many dislocations glide, it results in slip, the most common manifestation of plastic deformation in crystalline solids. The primary focus in this analysis of dislocation dynamics is on gliding motion.

#### SUPERPOSITION

The obtained analytical solutions for dislocations in Section 2.1.2 do not account for the presence of boundary conditions, but are only valid for an infinite domain. Present stresses should be incorporated in order to model plasticity at a microscale. A widely accepted method is the continuum-based approach, which starts with the combined infinite domain solution of all dislocations and then superposes the boundary conditions via an 'image' solution [7]. This is valid as long as no dislocations are actually on any boundaries, because the image field is a linear elastic field, and the values of the infinite domain solution can be assumed linear as well away from the plastic cores ($\approx 10\boldsymbol{b}$). The mathematical formulation is

$$\boldsymbol{\sigma} = \tilde{\boldsymbol{\sigma}} + \hat{\boldsymbol{\sigma}} \qquad \boldsymbol{\epsilon} = \tilde{\boldsymbol{\epsilon}} + \hat{\boldsymbol{\epsilon}} \qquad \boldsymbol{u} = \tilde{\boldsymbol{u}} + \hat{\boldsymbol{u}} \tag{2.11}$$

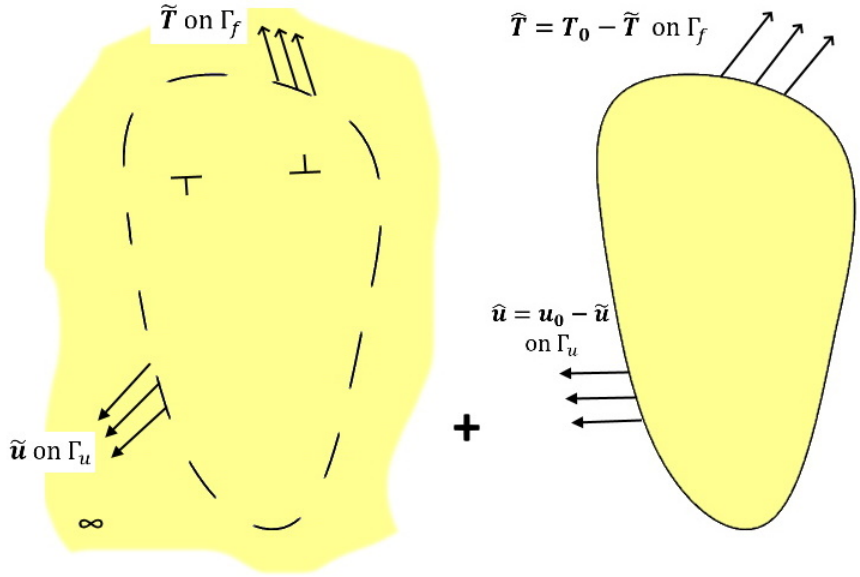


Figure 2.6: Principle of superposition illustrated. The total solution is decomposed into two. On the left is the analytical solution for $n$ dislocations in an infinite domain that give rise to certain displacement and tractions at the boundaries. On the right is the image solution, which is a bounded problem without any dislocations, but with the actual boundary conditions applied, and minus the tractions and displacements due to the dislocations in an infinite domain.

and it is illustrated in Figure 2.6. The (~) field contains the sum of all analytical stresses over $n_d$ dislocations, *i.e.*

$$\tilde{\boldsymbol{u}} = \sum_{i=1}^{n_d} \boldsymbol{u}_\infty \tag{2.12}$$

and the (^) image fields are chosen as such, that the stresses $\boldsymbol{\sigma}$, strains $\boldsymbol{\epsilon}$ and displacements $\boldsymbol{u}$ satisfy the boundary conditions. Because the singular fields can be solved exactly, the image problem that remains consists solely of smooth (^) fields and a simple FEM model suffices to solve it.

### FORCES AND STRESSES AROUND DISLOCATIONS

From Section 2.1.4 the stresses everywhere in the domain are known. Now the driving force acting on dislocation (I) is determined by the Peach-Köhler equation:

$$\boldsymbol{f}^{(I)} = \boldsymbol{t}^{(I)} \times \left[ \left( \hat{\boldsymbol{\sigma}} + \sum_{J \neq I} \boldsymbol{\sigma}_\infty^{(J)} \right) \cdot \boldsymbol{b}^{(I)} \right] \tag{2.13}$$

where $\boldsymbol{t}^{(I)}$ is the dislocation line direction as in Figure 2.3, $\hat{\boldsymbol{\sigma}}$ is the image stress due to boundary conditions and $\sum_{J \neq I} \boldsymbol{\sigma}_\infty^{(J)}$ is the sum of the stresses from all other dislocations, excluding its own stress field. For straight dislocations, we can describe the Peach-Köhler force as a purely configurational force. The components of the Peach-Köhler force are a gliding force in $x$-direction and a climbing force in $y$-direction. Climb requires vacancy diffusion, which happens at higher temperatures mostly and it is not considered in this study. Hence the glide component is driving for dislocations. The equation of motion of dislocation (I) can be put simply as follows.

$$m^{(I)} \dot{v}^{(I)} = f^{(I)} - f^{(I)}_{\text{resist}} \tag{2.14}$$

For a quasi-static framework the dynamics effects, such as inertia, can be neglected and the velocity changes for such short time scales (order of ~ ns [28]) are assumed irrelevant. The forces resisting the motion comprise of the Peierls-Nabarro stress and drag. They work in the direction opposing the dislocation velocity $v^{(I)}$. The Peierls-Nabarro stress is the friction stress that develops due to the breaking and forming of atomic bonds. It was found to be $b\tau_f$, with $\tau_f \approx 10^{-4}\mu$ (depending on the crystal structure). Drag arises in different forms such as electron drag, impurity effects, but primarily as phonon drag. Phonons are elastic waves in the lattice that oppose the velocity, which result in a net force $Bv^{(I)}$, where B is extracted from experiments or molecular

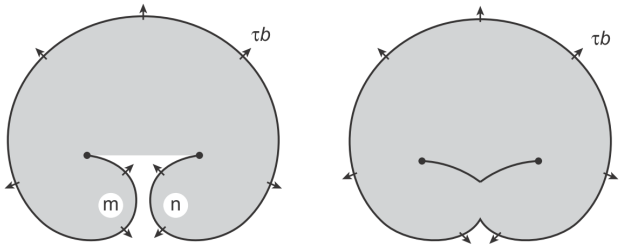


Figure 2.7: Global representation of the Frank-Read mechanism before and after dislocation nucleation. In the shaded area unit slip has occurred [24]

dynamics. When the phonon drag is the only resistance, the velocity can be calculated from the Peach-Köhler force, and the dynamic motion can be observed.

$$v^{(I)} = \frac{f^{(I)}}{B} \tag{2.15}$$

#### INTERACTION, GENERATION AND ANNIHILATION

After the early stages of deformation different slip planes and slip systems interact, which leads to work hardening. When a dislocation moves over the slip plane of another dipole it is called a forest interaction. Depending on the slip plane they can repel or attract. To prevent atomistic calculations, the general accepted idea is to apply a set of "rules" to govern these interactions. Attraction might lead to annihilation for oppositely signed dislocations. Sometimes it forms a junction, but more often a bound crossed state is formed, which is essentially a zero length junction. Junctions act as obstacles or pinning points for the dislocation motion [29]. Through the so-called Frank-Read mechanism a dislocation segment that is being pinned by two junctions or hard points can create new dislocations. Figure 2.7 shows a growing slip plane, due to a resolved shear stress $\tau$ and Burgers vector $b$ and which is blocked at both ends by some barrier or obstacle. The segments $m$ and $n$ annihilate [24].

## 2.2. COMPUTATIONAL METHODS

For solving boundary value problems the classical Finite Element Method (FEM) is around now for almost 70 years and it still is the go-to approach for solving most engineering problems. It is an important and necessary computational tool, as was already demonstrated in Section 2.1.4, but it is still limited to fixed meshes and linear elements and unable to capture discontinuities or singular stresses directly. An unified approach would combine the dislocation field with the boundary value problem. Of course the mesh can be modified around such irregularities, but because the dislocations move, it would require remeshing at every step. The prime focus of this chapter is therefore on alternatives such as X/GFEM and DE-FEM , where the approximation space itself is enriched with discontinuities, leaving the mesh unchanged, and their application to modelling dislocations.

### 2.2.1. X/GFEM

Enriching the standard formulation in Generalized FEM (GFEM), or eXtended FEM (XFEM), is based upon the concept of the partition of unity [10]. This property provides a framework to locally include *a priori* knowledge of the solution to the differential equation, such as discontinuities. Using the Galerkin formulation the displacement solution is discretised into a sum of shape functions and corresponding nodes. The general equation for X/GFEM is [30]

$$u^h(\boldsymbol{x}) = \underbrace{\sum_{i \in I_h} \varphi_i(\boldsymbol{x}) u_i}_{\text{std. FEM}} + \underbrace{\sum_{i \in I_h^*} \varphi_i(\boldsymbol{x}) \sum_{j}^{n} \psi_{ij}(\boldsymbol{x}) a_{ij}}_{\text{enrichment}} \tag{2.16}$$

where $I_h$ is the set of all nodes in the domain. $\psi(\boldsymbol{x})$ is the enrichment as function of $\boldsymbol{x}$. Each node $i$ is associated with a (local) shape function $\varphi_i$ and a degree of freedom, $u_i$ (dof). For X/GFEM the shape functions $\varphi_i$ are linear. A first analysis shows that Equation 2.16 has two parts. The standard part simply discretises the displacement solution to a set of linear interpolations per element $i$. The enrichments are

added locally to the enriched nodes $I_h^* \subseteq I_h$, to maintain the sparsity of the final stiffness matrix. Different enrichments can be applied per node, hence the sum over $n$ enrichments.

The enriched part is also multiplied with the linear shape functions $\varphi_i$, to make use of the partition of unity. The partition of unity states that the sum of the shape functions over the entire domain $\Omega$ is one:

$$\sum_{i \in I} \varphi_i(\boldsymbol{x}) = 1 \qquad \text{or more generally} \qquad \sum_{i \in I} \varphi_i(\boldsymbol{x}) f(\boldsymbol{x}) = f(\boldsymbol{x}). \tag{2.17}$$

This is also called the reproducing condition, because it allows to exactly reproduce any enrichment functions. And it means that without any enrichments present in Equation 2.16, X/GFEM reduces to standard FEM and the values at the nodes are computed exactly:

$$u^h(\boldsymbol{x}_i) = u_i. \tag{2.18}$$

This makes implementing boundary conditions very straightforward. Nevertheless, when a node is enriched, this property disappears. Therefore a common approach is to shift the enrichment, so that it vanishes at the nodes $\boldsymbol{x}_i$, *i.e.* $L_{ij}(\boldsymbol{x}) = [\psi_{ij}(\boldsymbol{x}) - \psi_{ij}(\boldsymbol{x}_i)]$. This is to maintain the so-called Kronecker-delta property from Equation 2.18 and to retain the physical meaning of the computed value at the nodes [11].

A disadvantage of X/GFEM is that the standard FE shape functions and the added enrichments may be linearly dependent. This can be solved by employing a perturbation approach [12]. Also, due to the added enrichments parasitic terms may spawn in the formulation, and thereby degrade the solution accuracy.

### MODELLING DISCONTINUITIES

As dislocations introduce discontinuities inside the material, it is useful to have a look at modelling discontinuities in X/GFEM. To accurately describe the locations $\boldsymbol{x}$ of discontinuities, the methodology of level sets is commonly used, where $f_\alpha = 0$ at the discontinuity [11, 31, 32]. A level set method adds dynamics to simple implicit surfaces, therewith preventing any parametrization [33]. Subsequently, at those locations both weak ($C^0$ continuous) and strong ($C^{-1}$ continuous) discontinuities can be incorporated into the FEM, depending on the type of enrichment function used. The Heaviside function

$$H(x) = \begin{cases} 0 & \text{for } x < 0 \\ 1 & \text{for } x > 0 \end{cases} \tag{2.19}$$

is a typical example for a $C^{-1}$ continuous function. The signed distance function is an example for a weak discontinuous function [32]. Although many enrichments are possible, some are definitely better than others in terms of computational efficiency and complexity. The combination gives the enrichment for Equation 2.16. For example, combining a signed distance function $f_\alpha$ (around discontinuity $\alpha$) with a Heaviside enrichment, gives

$$\psi_I(\boldsymbol{x}) = H(f_\alpha(\boldsymbol{x})) \tag{2.20}$$

and introduces a step function along the curve $f_\alpha(\boldsymbol{x}) = 0$ for node $I$. The choice of enrichment function depends of course on the expected behaviour of the displacement solution. Equation 2.20 works well for a bisected support, where the concerning element is cut entirely. For elements that contain the discontinuity tip (slit supports) other enrichments are better suited, such as [11]

$$\psi_I(\boldsymbol{x}) = \sum_\beta b_\beta(\boldsymbol{x}) \qquad \text{e.g.} \quad b_i(\boldsymbol{x}) = \left[ r \sin\frac{\theta}{2}, r^2 \sin\frac{\theta}{2} \right] \quad \text{where} \quad \theta(\boldsymbol{x}) = \tan^{-1}\left( \frac{f(\boldsymbol{x})}{r} \right). \tag{2.21}$$

This approach is easily extended to vector functions with discontinuities in direction $\boldsymbol{e}_t$ [11]:

$$\boldsymbol{u}(\boldsymbol{x}) = \sum_I \varphi_I\left(\boldsymbol{x}\right)\left(\boldsymbol{u}_I + a_I \boldsymbol{e}_t H(f(\boldsymbol{x}))\right). \tag{2.22}$$

A point of attention for modelling discontinuities is the integration of the local stiffness matrices, because normal Gauss quadrature requires smooth integrands. A common implementation is to decompose an element into so-called integration elements, which can be integrated separately. Alternatively the discontinuous part of the integrand can be replaced with an equivalent polynomial [16, 34], to allow for normal Gauss quadrature. This eliminates the need for creating extra integration elements, but requires other computational steps. Hence, in each case the integration of discontinuous elements requires careful implementation.

#### DE-FEM

Another approach to model discontinuities, similar to X/GFEM, is Discontinuity Enriched-FEM (DE-FEM) [19]. It is built on the same principle as Interface Generalized-FEM (IGFEM), where weak discontinuities are modelled using a generalized degree of freedom (dof) at the interface (or discontinuity) [35]. In the same manner, DE-FEM enables the modelling of both weak and strong discontinuities. The main difference with X/GFEM is that enriched dofs are no longer part of nodes from the original mesh, but are added along the discontinuities. This prevents any parasitic terms occurring in the blending elements and improves the solution accuracy. It also simplifies the kinematics for moving discontinuities, because the enriched discontinuity dofs are no longer coupled to the original mesh, but instead they are independent. The general formulation for the displacement field in DE-FEM is

$$\boldsymbol{u}^h(\boldsymbol{x}) = \underbrace{\sum_{i\in I_h} \varphi_i(\boldsymbol{x})\boldsymbol{u_i}}_{\text{std. FEM}} + \underbrace{\sum_{i\in I_w} \psi_i(\boldsymbol{x})\boldsymbol{\alpha_i}}_{\text{weak}} + \underbrace{\sum_{i\in I_s} \chi_i(\boldsymbol{x})\boldsymbol{\beta_i}}_{\text{strong}} \tag{2.23}$$

The enrichment functions $\psi$ and $\chi$ are used for weak and strong discontinuities, respectively, and they are constructed as a linear combination of the Lagrange shape functions in integration elements. Since they had to be computed anyway for the integration, this reduces the computational cost. Furthermore the displacement jump in $\chi$ is defined such that it has unit magnitude. This gives a physical interpretation to the associated enriched dofs $\boldsymbol{\beta}$. In the same manner $\boldsymbol{\alpha}$ can be physically interpreted as the magnitude in the gradient jump.

### 2.2.2. DISLOCATIONS WITH XFEM

In order to model dislocations in a two dimensional environment, the scope is limited to edge dislocations (screw dislocations operate out of plane). Their geometry can be broken down into a dislocation core, a Burgers vector $\boldsymbol{b^\alpha}$ and a glide plane (a line in a 2D environment), which normally connects two opposite dislocations, forming a dipole [9]. Slip along the glide plane is accomplished by adding an internal discontinuity to the displacement field. In accordance with Subsection 2.2.1, arbitrary discontinuities, such as the glide plane, can be modelled within each element exactly by Equation 2.22. The glide plane $f^\alpha(\boldsymbol{x})$ of dislocation $\alpha$ is then described as a level set function $f^\alpha(\boldsymbol{x}) = \alpha_0 + \alpha_j x_j$ (Einstein notation), and $f^\alpha(\boldsymbol{x}) = 0$ at the glide plane [13]. The internal discontinuity only applies in the direction tangential to the glide plane and with a given magnitude $b$, but without any degree of freedom. An example of such an resulting displacement approximation for dislocations is

$$\boldsymbol{u}(\boldsymbol{x}) = \sum_{I\in\mathscr{S}} \varphi_I(\boldsymbol{x})\boldsymbol{u}_I + \sum_{\alpha=1}^{n_D} b^\alpha \boldsymbol{e}_t^\alpha \sum_{J\in\mathscr{S}^\alpha} \varphi_J(\boldsymbol{x})\bar{H}(f^\alpha(\boldsymbol{x}))\psi(g^\alpha(\boldsymbol{x})) \tag{2.24}$$

for $n_D$ dislocations and $\mathscr{S}$ being the set of all the nodes [13]. $\mathscr{S}^\alpha$ is the set with enriched nodes and $\psi(g^\alpha(\boldsymbol{x}))$ is the core enrichment, which is discussed in the next section. Use of the symmetrized Heaviside function ($\bar{H}(z) = H(x) - \frac{1}{2}$) gives a more balanced approximation, because it centralises the discontinuity at the glide plane. As long as the jump has unit magnitude the length of the discontinuity is $b$.

#### CORE ENRICHMENT

Core enrichments are optional, because they only account for a very small portion of the entire dipole and compared to the slip plane, its influence is small. However, it allows for modelling more realistic core behaviour, when high accuracy calculations are required. In the core of a dislocation the displacement is discontinuous. Hence the strain is undefined or, in the case of the Heaviside function ($\psi(\boldsymbol{x}) = H(g(\boldsymbol{x}))$), singular. Consequently the cores need to be excluded for the strain energy calculation [9], or their energies need to be bounded through regularization. The core enrichment in Equation 2.24 works over another level set function $g^\alpha(\boldsymbol{x}) = \beta_0 + \beta_j x_j$ to localise the core. The intersection between $f^\alpha(\boldsymbol{x}) = 0$ and $g^\alpha(\boldsymbol{x}) = 0$ gives the core location. To regularize the core energy the derivative of the enrichment should be bounded. This can be done in various ways. A quantitative way is to adopt the tapered Somigliana dislocation, but other enrichments have been applied as well [13–15].

#### PEACH-KÖHLER FORCE

As described in Subsection 2.1.4 the presence of a dislocation generates internal stresses. In superposition methods, the acting stress upon a dislocation was given by the image stresses (external stresses including

boundaries) and the other dislocations, but excluding its self-stress:

$$\bar{\boldsymbol{\sigma}} = \hat{\boldsymbol{\sigma}} + \sum_{J \neq I}^{n_D} \boldsymbol{\sigma}^{(J)}. \tag{2.25}$$

These stresses induce the Peach-Köhler force, given by Equation 2.13. However, for enriched formulations the computed stress field follows directly from the computed displacement field and therefore comprises all stresses, including its own stress field as well. A solution might be to try and subtract the (infinite domain) analytical solution. As long as the dislocation is far enough from the boundary, this is a valid assumption (see the $\frac{1}{r}$ dependency in eq. 2.4). Another problem is the accuracy of the computed stress at the core, which requires a sufficient resolution of the FEM to calculate the Peach-Köhler force. A solution to this problem is to compute the Peach-Köhler force by using an Eshelby contour integral, or the so-called J-integral [20, 26]. This approach is based on a more rigorous definition, that the self-force of a dislocation can be expressed as the gradient of the strain energy with respect to the dislocation position [36, 37]. However, this J-integral still requires a domain of radius $3h$, which leads to very fine meshes if interaction between dislocations should also be modelled correctly [14]. Aforesaid evaluation of the Peach-Köhler force is primarily useful for complex geometries and inclusions, where simple superposition is cumbersome. Another proposed approach is to introduce a singular core enrichment based on the infinite domain solution, limited to a bounded area around the dislocation core [14]. This enrichment increases the accuracy of the stress field near the core, and improves the Peach-Köhler force calculation.

# 3

# STATIONARY DISCRETE DISLOCATIONS

The first step of simulating discrete dislocation dynamics with Discontinuity-Enriched FEM (DE-FEM) is modelling a stationary dislocation in 2D. This is done in a similar manner as in X/GFEM by breaking down a dipole into two edge dislocations and a slip plane. This is proven to be a viable alternative to the superposition method or X/GFEM, yielding an accurate displacement field with a simple, elegant formulation. The numerical convergence is demonstrated and different approaches for retrieving the stress field around a single dislocation are discussed.

## 3.1. TWO-DIMENSIONAL SCOPE

Because the goal of this research is to find a way to capture discrete dislocation dynamics with DE-FEM, the initial scope is limited to 2D dislocations to test and demonstrate the principle. The boundary between a slipped region of atoms and the normal lattice is the 3D dislocation loop. From a 2D perspective, this loop reduces to two point dislocations with a plane in-between, which undergoes a shift. It can be seen by cutting the disc in Figure 2.3(c) vertically. Screw dislocations are therefore excluded from the analysis, because their displacement is out-of-plane. Instead, the main focus is on edge dislocations with in-plane displacements and stresses. Boundary conditions will be applied in-plane, and the out-of-plane strains are assumed to be negligible, thus enabling the use of plane strain conditions, as was discussed in Section 2.1.2. Henceforth, when dipoles are considered, it refers to two oppositely signed edge dislocations in 2D connected by a slip plane.

## 3.2. FORMULATION

Following the same principle as discussed in Section 2.2.2 [9], each dislocation is treated as part of a dipole and modelled as an arbitrarily oriented straight plane with the Burgers vector $\boldsymbol{b}^\gamma$ enforced as displacement jump tangentially over the glide plane, as shown in Figure 3.1. Each core is initially modelled with a weak enrichment only, without any special singular core treatment. Because of the weak enrichment, a jump in the gradients, the different kinematic fields from the slipped and unslipped region are allowed to merge. The absence of a singular treatment indicates that the cores are not modelled for any singular behaviour, but to merely ramp the displacement discontinuity. Since DE-FEM allows for adding discontinuous enrichments in a local space, it is ideally suited for these kind of problems. The original DE-FEM formulation (Equation 2.23), then becomes

$$\boldsymbol{u}^h(\boldsymbol{x}) = \sum_{i \in I_h} \varphi_i(\boldsymbol{x}) \boldsymbol{u_i} + \sum_{\gamma=0}^{n_D} \left( \sum_{i \in I_w^\gamma} \psi_i(\boldsymbol{x}) \boldsymbol{\alpha_i} + \sum_{i \in I_s^\gamma} \chi_i(\boldsymbol{x}) \boldsymbol{b}_i^\gamma \right), \tag{3.1}$$

where $n_D$ is the number of dipoles, and $I_w^\gamma$ and $I_s^\gamma$ refer to the index set of strong and weak nodes respectively associated with dislocation $\gamma$. Note that, even though each dipole consists of two oppositely signed dislocations, their shared slip plane (the connecting line) has as constant Burgers vector. Hence, the strong nodes have a prescribed displacement jump at the given locations, while the weak nodes are unconstrained, allowing different kinematic fields at each side of the slip plane. The requirement for weak nodes could be argued


Figure 3.1: Schematic breakdown of a dipole with two 2D edge dislocations in purple and with opposite signs, and the glide plane in 2D as line in orange, defined for a positive $\boldsymbol{b}$ from left to right. The arrows show the displacement field around the dipole. This convention is used throughout this report.

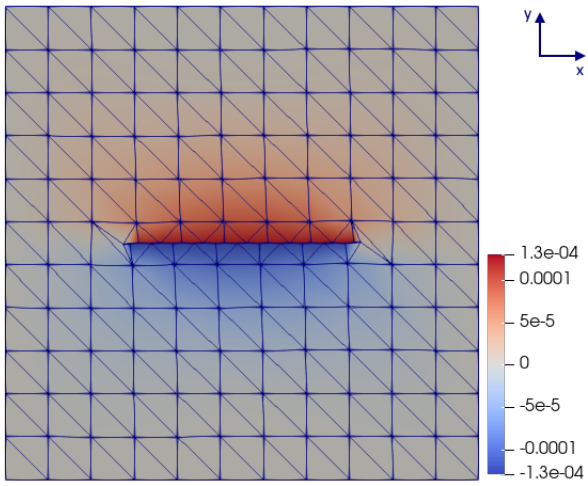


Figure 3.2: (Cover picture) The horizontal displacement in µm for a DE-FEM modelled dipole with clamped boundary conditions. The domain is 2 µm × 2 µm and the jump $|\boldsymbol{b}| = 0.25$ nm. The jump is augmented ~ 200 times to illustrate the working principle.

from a physical perspective, since the crystallographic orientations are similar over the slip plane. However, they are included for improved accuracy of the numerical solution. For a square domain of 2 µm × 2 µm, $|\boldsymbol{b}| = 0.25$ nm, E = 70 GPa and $\nu = 0.33$ (aluminium) and with homogeneous essential boundary conditions the result is shown for one dipole in Figure 3.2 with the displacement discontinuity augmented to clearly see the design principle.

## 3.3. VERIFICATION AND ERROR NORMS

Verification is done by comparing the results with the analytical displacement relations, as stated by Equation 2.5 - 2.6 [6] and plotted in Figure 3.3 with both $x$ and $y$-displacement as vector plot for an infinite domain. In order to use these relations to verify the DE-FEM solution, the analytical values are prescribed as boundary conditions, *i.e.*, numerically mimicking an unbounded solution:

$$\text{B.C.}: \quad \boldsymbol{u_0} = \tilde{\boldsymbol{u}} \text{ on } \Gamma_u \qquad \text{where} \qquad \tilde{\boldsymbol{u}} = \sum_{i=1}^{n_d} \boldsymbol{u}_\infty. \tag{3.2}$$

where $\boldsymbol{u^0}$ denotes the applied essential boundary conditions, $\Gamma_u$ all four boundaries of the 2D domain and $\boldsymbol{u}_\infty$ is the unbounded analytical expression. These kind of boundary conditions will henceforth be called "boundaryless", because they mimic part of the infinite space and allow direct comparison with the exact analytical solution.

Various norms for quantifying the error exist, such as the $\mathscr{L}^2$ norm and the energy norm. But because verification is done using the analytical relations, it is important to note that within a radius of $10 \cdot \boldsymbol{b}$ of the singularity, they are no longer valid, because the assumption of linear elasticity no longer holds. Hence, very close to the singularity the exact values cannot be used. To demonstrate the (in)validity of the different norms, they are integrated over an area that contains the singularity for the exact solution. For the $\mathscr{L}^2$ norm and the energy norm to be of use, the analytical displacement and stress functions should be square integrable over the entire domain. If singular they are not valid for any error computation. The $\mathscr{L}^2$ norms for both functions over the core are checked for the $\mathscr{H}^1$ and the $\mathscr{H}^{1-\epsilon}$ space:

$$f^{\mathscr{L}^2}_{\text{norm}} = \sqrt{\int_0^{2\pi}\int_0^1 \left(f(r,\theta)\right)^2 r\,\mathrm{d}r\,\mathrm{d}\theta} \quad \text{or} \quad \sqrt{\int_{-1}^{1}\int_{-1}^{1}\left(f(x,y)\right)^2 \mathrm{d}x\,\mathrm{d}y} \tag{3.3}$$

$$f^{\mathscr{L}^{2-\epsilon}}_{\text{norm}} = \sqrt[1.99]{\int_0^{2\pi}\int_0^1 \left(f(r,\theta)\right)^{1.99} r\,\mathrm{d}r\,\mathrm{d}\theta} \quad \text{or} \quad \sqrt[1.99]{\int_{-1}^{1}\int_{-1}^{1}\left(f(x,y)\right)^{1.99} \mathrm{d}x\,\mathrm{d}y}. \tag{3.4}$$

Because the nature of the singularity in the stress relations is $1/r$, they are expressed in polar coordinates, for ease of use in Equations 3.5 and 3.6:

$$\sigma_{rr} = \sigma_{\theta\theta} = -\frac{b}{2\pi(1-\nu)}\frac{1}{r}\sin(\theta) \tag{3.5}$$

$$\sigma_{r\theta} = \frac{b}{2\pi(1-\nu)}\frac{1}{r}\cos(\theta) \tag{3.6}$$

The results are shown in Table 3.1. As expected the $1/r$ singularity causes the $\mathscr{L}^2$-norm of the analytical stress to diverge, which indicates that the solution of the problem is not to be found in the regular $\mathscr{H}^1$-space. The $\mathscr{L}^2$ error in the stresses is equivalent to the error in the energy norm as they both contain the inner product of the strains. The stresses do converge for the $\mathscr{L}^{2-\epsilon}$-norm, indicating that the solution lies in the $\mathscr{H}^{1-\epsilon}$-space. Therefore, as long as the cores are included, the energy norm cannot be used as a verification method for the solution. The norm over the displacements on the other hand is square integrable, because the analytical relation converges. Hence, the $\mathscr{L}^2$ norm over the displacements will be a viable convergence test for verification of the numerical solution. Because the square root of the arctan is only defined equally around the origin, the $\mathscr{L}^{2-\epsilon}$-norm for the displacements are not shown in the table.

Table 3.1: Various norms of the analytical relations around a dislocation

| $f=$ | $u_1(x,y)$ | $u_2(x,y)$ | $\sigma_{rr}(r,\theta)$ | $\sigma_{\theta\theta}(r,\theta)$ | $\sigma_{r\theta}(r,\theta)$ |
|---|---|---|---|---|---|
| $L^2(\Omega)$ | $5.74\cdot10^{-5}$ | $1.53\cdot10^{-4}$ | $\infty$ | $\infty$ | $\infty$ |
| $L^{2-\epsilon}(\Omega)$ | - | - | 0.0217 | 0.0217 | 0.0217 |

## 3.4. CONVERGENCE RATES

The next step in verification is the convergence analysis of the error norms with increasing mesh refinement. Use of the error in the energy norm makes no sense, as was demonstrated before, unless one were to exclude the dislocation cores form the strain energy summation. Here the convergence of the error in the $\mathscr{L}^2$-norm is demonstrated. The $\mathscr{L}^2$-norm of the error in the displacements is defined as

$$\left\|\boldsymbol{u}-\boldsymbol{u}^h\right\|_{\mathscr{L}^2(\Omega)} = \sqrt{\frac{\sum_{e\in\Omega}\int_e \left\|\boldsymbol{u}-\boldsymbol{u}^h\right\|^2 \mathrm{d}\Omega}{\sum_{e\in\Omega}\int_e \|\boldsymbol{u}\|^2 \mathrm{d}\Omega}}, \tag{3.7}$$

where $\boldsymbol{u}^h$ is the numerical solution, $\boldsymbol{u}$ the exact solution, $\Omega$ the entire domain over which the $\mathscr{L}^2$-norm is taken, and $e$ an element inside $\Omega$.

First, the norm is computed for a numerical field of $31\times31$ elements with three arbitrarily placed dipoles, and shown per element in Figure 3.4. Note again, that the boundary conditions are set as the superposition of the analytical infinite domain relations, thus mimicking an infinite space. The errors in the $\mathscr{L}^2$-norm are very low and mainly occur close to the dislocations, where the exact solution is most non-linear.

The convergence rate is computed for a simple problem consisting of one dipole, or two dislocations, inside a 2 µm × 2 µm domain with parameters $|\boldsymbol{b}| = 0.25$ nm, E = 70 GPa and $\nu = 0.33$. The boundary conditions are set "boundaryless", as Equation 3.2. The total error in the $\mathscr{L}^2$-norm is computed for differently sized triangular meshes (*i.e.* 7×7, 15×15, 31×31, 63×63, 127×127) and shown in Figure 3.5. The a priori error estimate for algebraic convergence rate can be computed as

$$\left\|\boldsymbol{u}-\boldsymbol{u}^h\right\|_{L^2(\Omega)} \leq C_1 N^{\beta_N} \|\boldsymbol{u}\|_{L^2(\Omega)} \tag{3.8}$$

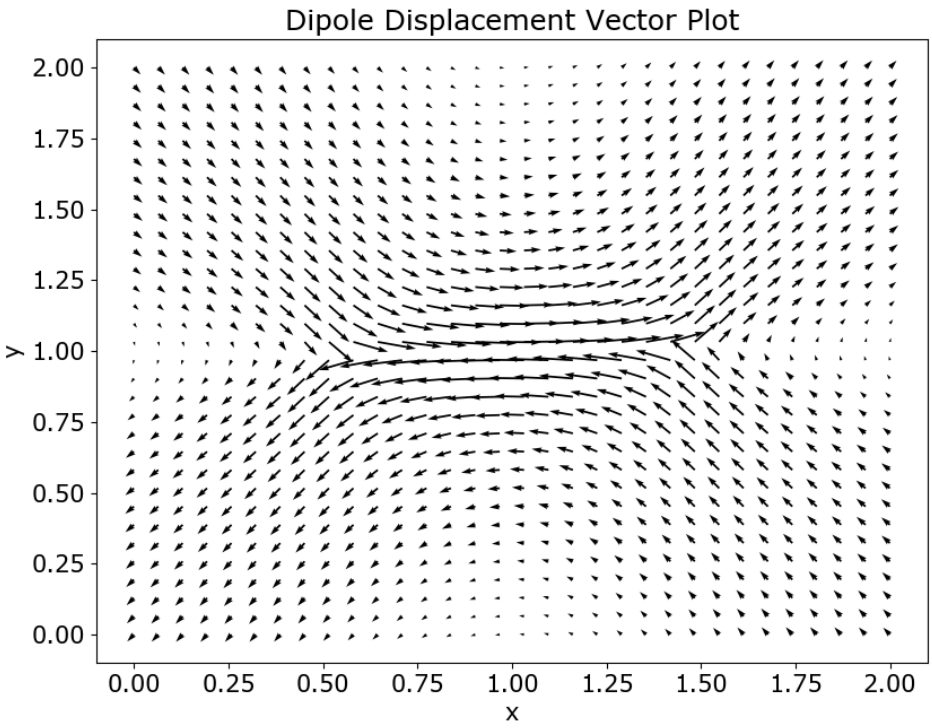


Figure 3.3: The in-plane displacement of the analytical infinite domain solution. The relative jump over the slip plane is 0.25 nm

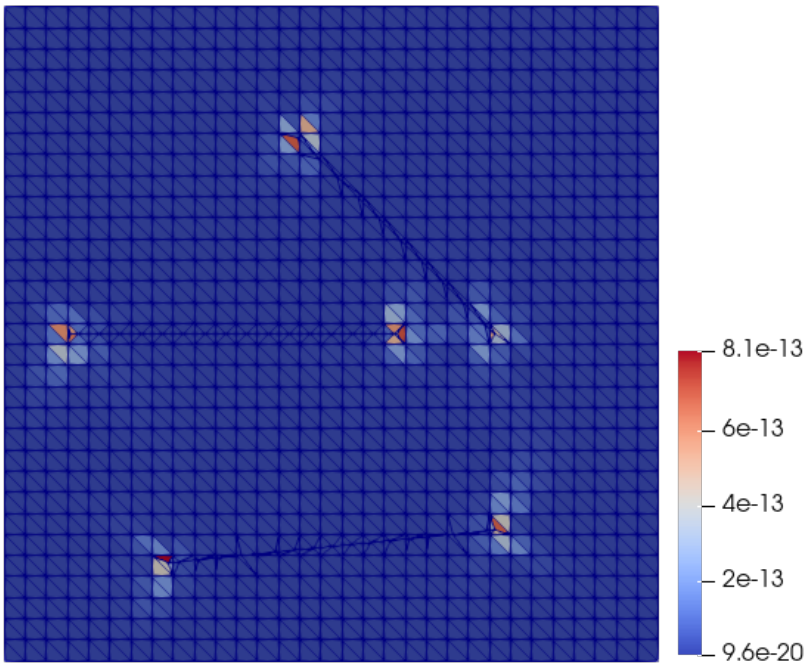


Figure 3.4: The local squared error for an artificially unbounded field of $31 \times 31$ elements with three slanted dipoles.

where number of degrees of freedom (dofs) $N$ is roughly related to the inverse square of the mesh size $1/h^2$, $C_1$ is some constant and $\beta_N$ is the convergence rate. Because DE-FEM uses extra dofs to represent the crack, or the dislocations in this case, the convergence rates are computed with respect to the number of dofs. With a value of $-0.49$ the convergence in the $\mathscr{L}^2$ error norm is not optimal, but is as good as can be expected for a discontinuous displacement field.

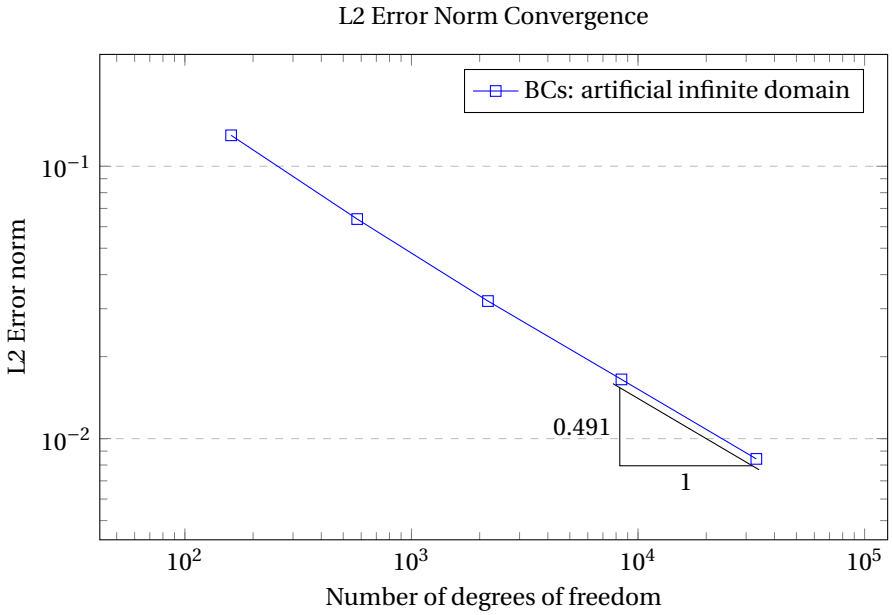


Figure 3.5: Convergence of the $\mathscr{L}^2$-norm of the error vs. number of degrees of freedom

## 3.5. STRESS ANALYSIS

Close to the cores the stresses are highly non-linear and verification with the analytical solution is not possible. However, a proper understanding of the numerical singularity in the stresses is essential before moving on to the dynamics of discrete dislocations. To what extent are the numerically computed stresses sound, and what is their short-range and long-range influence on the total stress field? To this end a single dislocation is modelled in different ways and the stress field around it is investigated.

### 3.5.1. INITIAL ANALYSIS

For a single dipole inside a "boundaryless" field the analytical and numerical stress fields are shown in Figure 3.6 and 3.7, respectively. it shows the stress fields are very similar. To better illustrate the long-range stress field, the sensitivity of the colour mapping is increased though and the short-range stresses are much higher than the 20 MPa from the figures. Close to the core the differences are significant, as is also discussed in the next chapter. It is also important to note that the numerical stress is initially known roughly at the element level, because they follow directly from the gradients, which are constant at (integration) element level in DE-FEM. Figure 3.8 shows both this original roughness at the element level, as well as the inability of the linear shape functions to capture the non-linear core stresses accurately. Only by use of advanced interpolation techniques [38] is the smooth stress field in figures 3.6 and 3.7 obtained.

### 3.5.2. SINGLE DISLOCATION STRESS

To better understand the numerical stress field, the field is ideally compared with a single analytical dislocation. Also for the computation of the Peach-Köhler force it is important to know the individual contributions of each dislocation to the global field. So far only dipoles have been modelled and each dislocation is created as the start or the end of the slipped region. Therefore three ways of modelling a single edge dislocation are proposed to analyse the influence of a single numerical dislocation. The first approach removes one of the dislocations and extends the slip plane to the boundary, as illustrated in Figure 3.9. The second approach

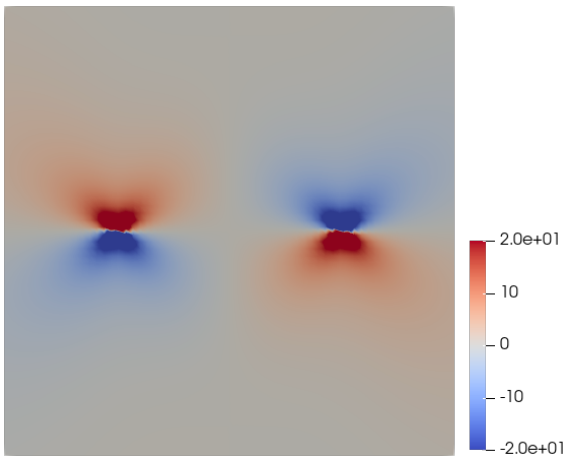


Figure 3.6: Exact analytical field in an infinite domain, stress component $\sigma_{11}$ in MPa. The colouring of the figure is scaled down to show the long-range stress field. The actual stresses around the dislocations are several orders of magnitude larger.

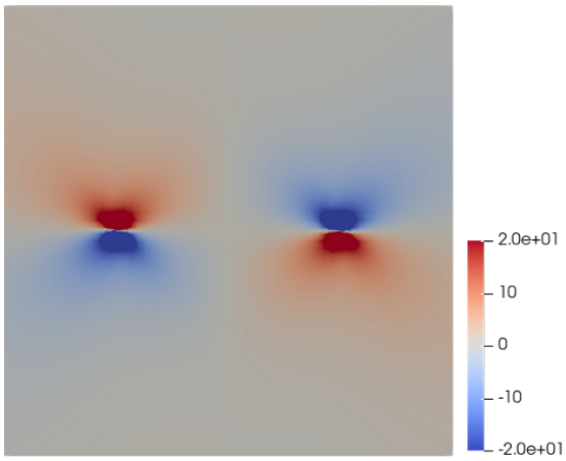


Figure 3.7: Numerical field for 31x31 elements, stress component $\sigma_{11}$ in MPa. The colouring of the figure is scaled down to show the long-range stress field. The actual stresses around the dislocations are several orders of magnitude larger.

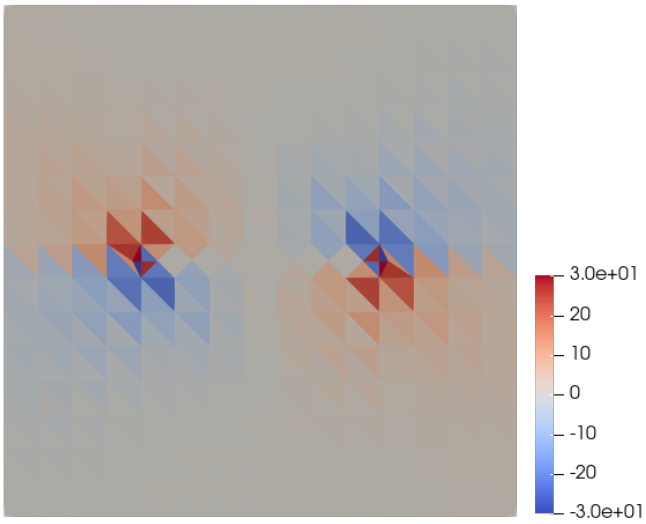


Figure 3.8: The numerical field for the $\sigma_{11}$ stress component on a 15 × 15 mesh. The stresses in MPa are computed by the gradients and therefore known at element level. A rougher mesh is used than before to clearly show the numerical, irregular high stresses around the dislocations. It shows that interpolation is required in order to simulate smooth dislocation dynamics.

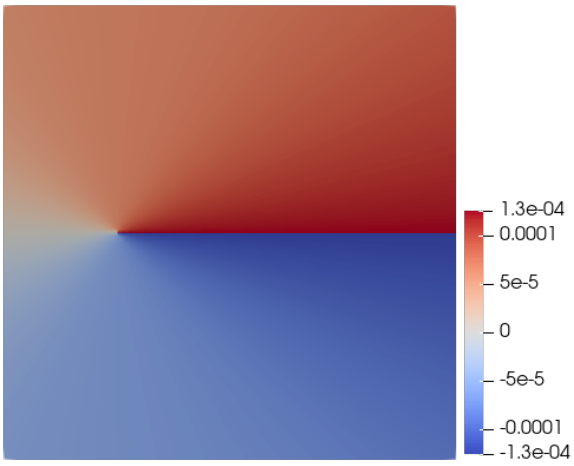


Figure 3.9: The horizontal displacement in µm. A single dislocation modelled by a single slip plane with $\|\boldsymbol{b}\| = 0.25$ nm in $x$-direction. Here with "boundaryless" boundary conditions.

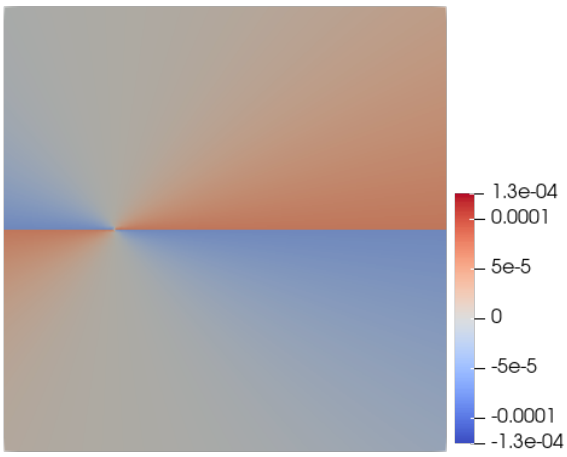


Figure 3.10: The horizontal displacement in µm. A single dislocation modelled by a two opposite slip planes with $\|\boldsymbol{b}\| = 0.125$ nm each (in $x$-direction and $-x$-direction). Here with "boundaryless" boundary conditions.

better mimics the exact analytical displacement relation by removing the influence of the other dislocation at the other end as well. It extends the slip plane to both boundaries, but with half of the Burgers vector $\boldsymbol{b}$ each, as in Figure 3.10. Although they look quite different, the main difference is an integration constant in the displacement, and the stresses of both fields are identical from an analytical perspective, and very similar from a numerical perspective.

The third approach is to find a Least Squares fit to one of these numerical stress fields using non-linear regression. This fit is basically an analytical relation, but based on the numerical stress field. The fitted polynomial for each of the components of the stress is

$$\frac{a + bx + cy + dxy + ex^2 + fy^2 + gx^2y + hy^2x + ix^3 + jy^3}{(x^2 + y^2)^2}. \tag{3.9}$$

and the parameters $a - j$ have to be found for every mesh. The equation can be simplified by retaining only $g$ and $j$ for $\sigma_{11}$ and $\sigma_{22}$, and $h$ and $i$ for $\sigma_{12}$, as the fit is closer to the analytical solution (*cf.* Equations 2.8-2.10), but keeping all parameters gives a better overall fit to the numerical field.

To compare these stress fields, they are all computed for a single dislocation located at $X = (0.5, 1.0)$ in a 2 µm × 2 µm domain with "boundaryless" boundary conditions. The values for the different stress components are evaluated over the horizontal line $y = 1.02$, just above the glide plane, as shown in Figure 3.11, and plotted in Figure 3.12 - 3.14. Near the core differences are significant, but far away all solutions converge to the exact solution. To measure the accuracy of the stress fields, the Root Mean Square Error is computed over all the nodes $n$ inside the domain $\Omega$ compared to the exact solution:

$$RMSE = \sqrt{\frac{\sum_{i=0}^{n} \epsilon^2}{n}} \tag{3.10}$$

where $\epsilon$ is the error in the stress value at node $i$ and $n$ the number of nodes.

Table 3.2 shows the results for these three approaches, for all the nodes in the domain $\Omega$ and for the case where the nodes in a radius of 0.2 µm around the dislocation core are excluded. Out of the first two approaches, the second one, with two antisymmetric glide planes, was chosen to best approximate the exact stress. Therefore also the third approach (the fitted least squares function *or* the fit), was computed based on the stress field of the second approach.

When all stresses over the entire domain are included, the error is lowest for the third approach, *i.e.*, the fit. This makes sense, because both the fit and the exact solution are analytical functions with an equivalent singularity, which are unaffected by mesh roughness. However, if one were to exclude those cores from the

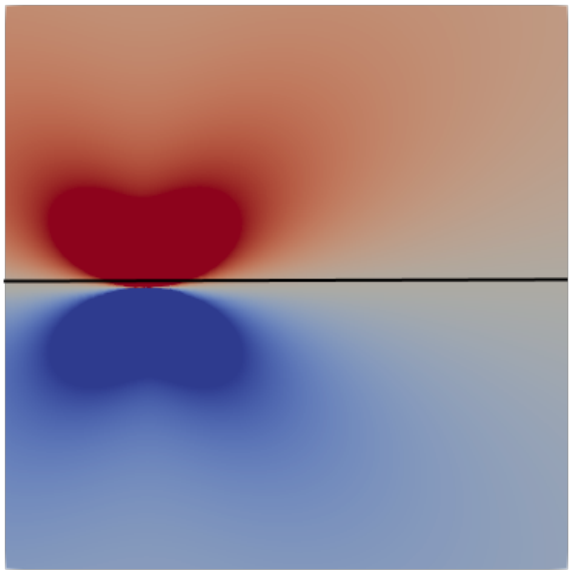

Figure 3.11: Evaluating the stresses over the black line at $y = 1.02$, slightly above the triangular elements cut by the glide plane, but still close to the singularity.

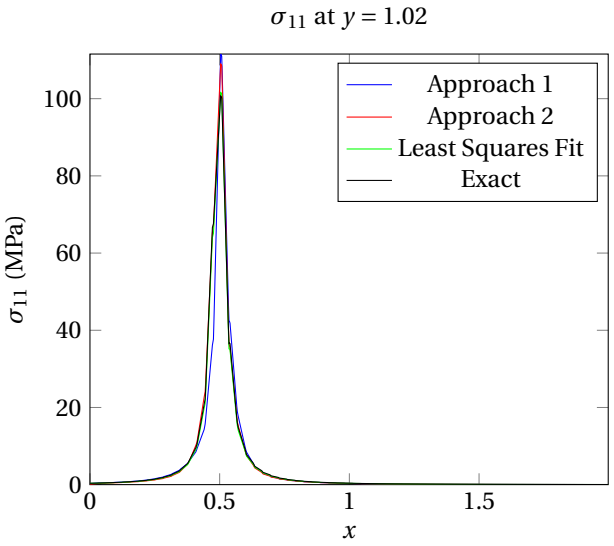


Figure 3.12: Stress component $\sigma_{11}$ for the three different approaches and the exact infinite domain solution at $y = 1.02$

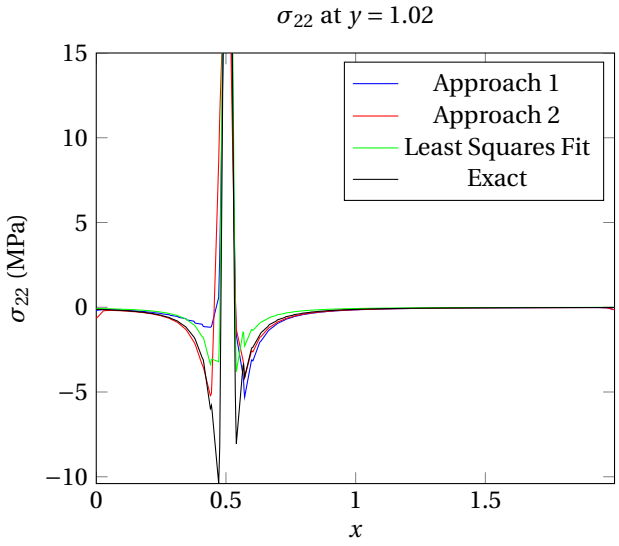


Figure 3.13: Stress component $\sigma_{22}$ for the three different approaches and the exact infinite domain solution at $y = 1.02$

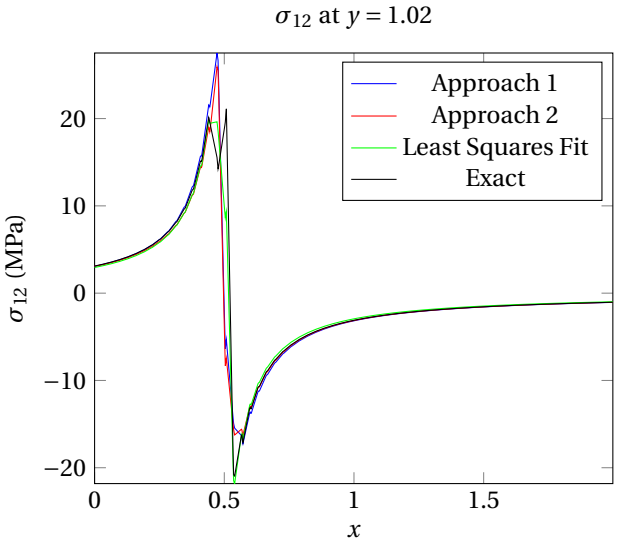


Figure 3.14: Stress component $\sigma_{12}$ for the three different approaches and the exact infinite domain solution at $y = 1.02$

Table 3.2: Root Mean Square Error for the error of different stress components with respect to the exact analytical solution. The first case considers all nodes in the domain from 2 µm × 2 µm and the second case excludes the nodes within a radius of 0.2 µm around the dislocation.

| | Entire domain $\Omega$ | | | Domain $\Omega$ excl. cores | | |
|---|---|---|---|---|---|---|
| | $\boldsymbol{\sigma_{11}}$ | $\boldsymbol{\sigma_{22}}$ | $\boldsymbol{\sigma_{12}}$ | $\boldsymbol{\sigma_{11}}$ | $\boldsymbol{\sigma_{22}}$ | $\boldsymbol{\sigma_{12}}$ |
| $RMSE$(Approach 1) | 1.21 | 0.46 | 2.57 | 0.08 | 0.021 | 0.012 |
| $RMSE$(Approach 2) | 0.096 | 0.326 | 3.274 | 0.008 | 0.007 | 0.005 |
| $RMSE$(Fit) | 0.052 | 0.322 | 0.363 | 0.011 | 0.013 | 0.015 |

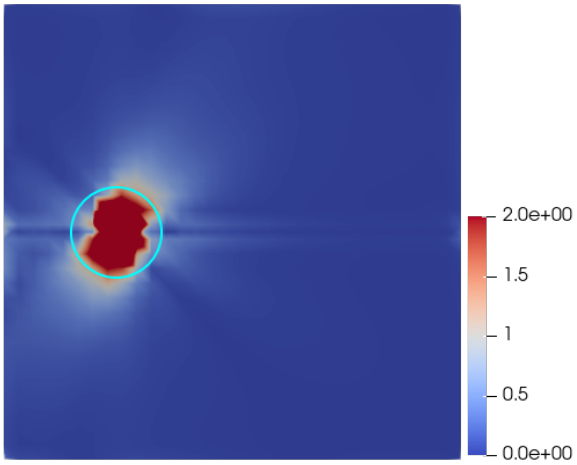


Figure 3.15: The magnitude of the error in the stresses for the second approach. Here with 'boundaryless' boundary conditions. The core region with r=0.2 µm is indicated with cyan.

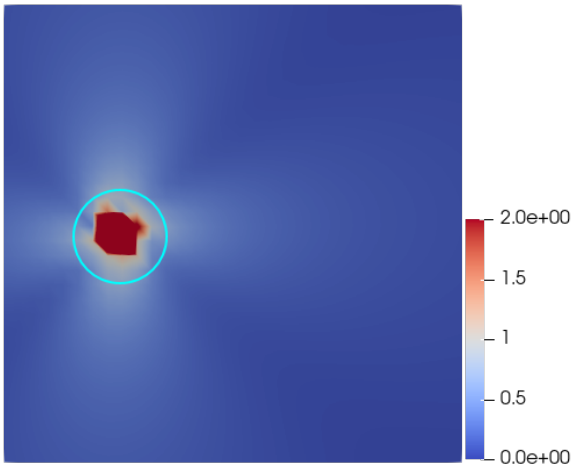


Figure 3.16: The magnitude of the error in the stresses for the fit, based on the stress field from the second approach. The core region with r=0.2 µm is indicated with cyan.

error computation, the second approach has the lowest errors. So, although the fit nicely approximates the artificial singularity, the second approach is better for the long-range stress field. This is also demonstrated in figures 3.15 and 3.16, where the local error (with respect to the analytical solution) is plotted for the second approach and the fitted solution, respectively. The fit has lower short-range errors, but higher long-range errors.

# 4

# DISCRETE DISLOCATIONS DYNAMICS

The movement of multiple dislocations is governed by the Peach-Köhler force. Because this follows directly from the stress field, accurate stress retrieval is a crucial step for simulating discrete dislocation dynamics. And because the Peach-Köhler force is a configurational force, as was explained in Subsection 2.1.4, a dislocation moves due to its surroundings, such as other dislocations and applied boundary conditions, but excludes the (singular) self-stress. In the numerical solution only the total stress is known due to applied boundary conditions and *all* dislocations. In this chapter various methods are discussed to separate the self-stress from the rest, yielding the configurational stress. Also the combination of a core enrichment with DE-FEM is investigated, but it turned out to be quite cumbersome. Hence, an alternative approach to tackle discrete dislocation dynamics with DE-FEM is presented, where DE-FEM is combined with the superposition approach.

## 4.1. ELIMINATING THE SINGULARITY

The first attempt of separating the self-stress from the rest of the stress field is to subtract the known analytical stress field of a single dislocation in an infinite domain from a patch of elements. Although the numerical values are never actually singular, the strains and stresses keep on increasing with mesh refinement. This happens because the displacement discontinuity is constant, but the integration elements around the dislocation decrease in size and increase in strain. This will be referred to as a numerical singularity, even though the values are not actually singular.

This is demonstrated in Figures 4.1 and 4.2, where the values are obtained from a "boundaryless" field of 2 µm × 2 µm with two dislocations, as shown in Figure 3.6. For this case, the Peach-Köhler stress of the left dislocation should consists solely of the stress due to the right dislocation and is therefore known to be [0, 0, -1.56] MPa (Voigt notation). Figure 4.1a) shows that the numerical shear stress values near the core (at $\Delta y = +0.02$) are increasing with mesh refinement, and surpassing the analytical solution in magnitude. It illustrates the difficulty of nullifying the numerical singularity with the analytical description. Also the initially known element stresses are plotted, which again emphasizes the importance of interpolation to smoothen the field. However, both are unable to accurately capture the core behaviour. Further away from the core the numerical approximation gets better and better. If one were to take a contour with radius 0.1 µm around the dislocation, the numerical estimates are already much closer to the exact solution, as is shown in Figure 4.1b).

In order to subtract an analytical function from a numerical field, a patch of values needs to be clearly defined. As long as the values close to the core are considered, any numerical estimation will exceed the analytical solution. Furthermore, the element stress values are too coarse and subtracting from these could lead to heavy fluctuations in the stresses with only small changes in location. Therefore the analytical solution is subtracted from the smooth interpolated stress values at a radius r=0.1 and 0.2 µm away from the core. The results for finer and finer meshes are shown in Figure 4.2. For r=0.1 µm very fine meshes are required to come close to a correct prediction, but also for a relative large radius of r=0.2 µm the fluctuations are still significant. In a simulation problem, even the smallest errors can increase over time very quickly. Because of these variations and the required large radius around the dislocation, it was concluded that direct computation of the Peach-Köhler stress by subtracting the analytical solution is not possible in this formulation. Either the nu-

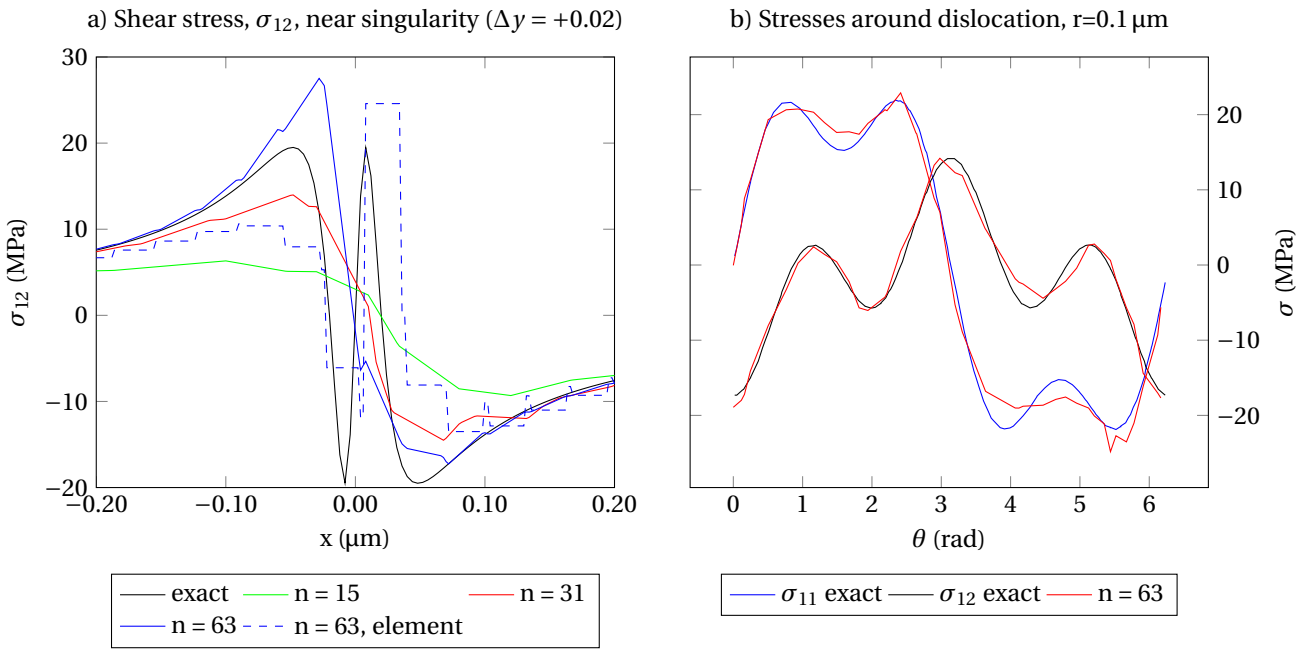


Figure 4.1: On the left the interpolated shear stress component, $\sigma_{12}$, is plotted over the line $y = 1.02$ for differently sized meshes. For the finest mesh, also the initially computed element stress is plotted. On the right both $\sigma_{11}$ and $\sigma_{12}$ components are plotted over a contour around one of the numerical dislocations for a "boundaryless" domain with two dislocations on a 63 × 63 mesh and compared to the analytical relations.

merical stresses have to be more accurate, or a different approach of removing the self-stress of the numerical singularity is required.

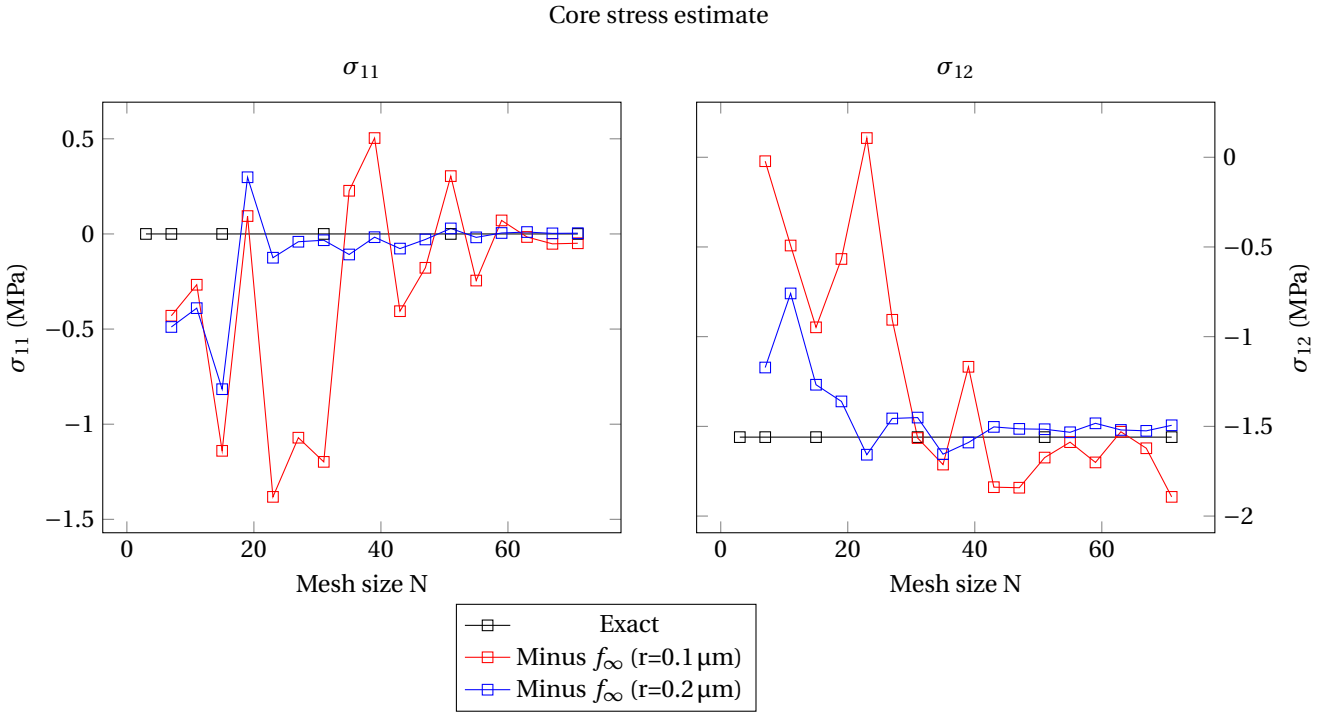


Figure 4.2: The core stress estimates by subtracting the analytical function, $f_\infty$, from the interpolated stress values around the core at two different radii: r=0.1 µm and r=0.2 µm. It is compared to the (analytically) known Peach-Köhler stress, *i.e.*, the stress of the other dislocation.

Unfortunately the fitted least squares field, constructed in section 3.5.2 from a numerical solution, does

not work either, because it is constructed as function similar to the exact analytical solution. And because it has the same kind of analytical singularity, it is unable to correctly predict this numerical singularity as well. Ideally the entire domain of integration elements would be built for each dislocation only to accurately identify the numerical self-stress around the singularity and to be able to remove this self-stress from the rest of the field. This idea is further pursued in Section 4.3.

## 4.2. CORE ENRICHMENT

Because the analytical and numerical solutions are not easily mixed afterwards, another approach is to incorporate the analytical singularity in the numerical solution. This way the DE-FEM formulation is enriched even further with the singularities to be able to represent the dislocations very accurately and to improve the stresses near the core. This method is henceforth called Discontinuity- and Core-Enriched FEM (DCE-FEM). It is inspired by the work of Gracie in modelling dislocations with X/GFEM [14], but instead of fixing the core formulation for a dislocation, a new degree of freedom is directly associated with the weight of the singular enrichment, so afterwards its importance can be evaluated with respect to the standard DE-FEM formulation. Plus, it gives an indication for the strength of the singularity and what fraction of the singular solution is to be subtracted to exclude the self-stress.

### 4.2.1. FORMULATION

For the choice of singular enrichment function the analytical infinite domain solution is chosen, similarly to [14], because it already has the desired behaviour and it can possibly be used later on to compute the Peach-Köhler force directly. The core enrichment follows directly from Equations 2.5 and 2.6:

$$\boldsymbol{f}^{\gamma}_{\text{exact}}(\boldsymbol{x}) = \begin{pmatrix} \left(\frac{b^{\gamma}}{2\pi(1-\nu)}\left[\frac{1}{2}\frac{x_1 x_2}{x_1^2+x_2^2} - (1-\nu)\arctan\left(\frac{x_1}{x_2}\right)\right]\right)\boldsymbol{e}_t \\ \left(\frac{b^{\gamma}}{2\pi(1-\nu)}\left[\frac{1}{2}\frac{x_2^2}{x_1^2+x_2^2} - \frac{1}{4}(1-2\nu)\ln\left|x_1^2+x_2^2\right|\right]\right)\boldsymbol{e}_n \end{pmatrix}. \tag{4.1}$$

Note that $\boldsymbol{e}_t$ and $\boldsymbol{e}_n$ are the normal and tangential unit vectors to the slip plane, because the core enrichment should be aligned with it. Also, the two dislocations within one dipole are oppositely signed, so each dislocation has its own core enrichment.

Within X/GFEM these enrichments are localized using the partition of unity. In DCE-FEM the core enrichment is a stand-alone term, so for each dipole $\gamma$ there are two dislocations, $\gamma_1$ and $\gamma_2$, each with their own core enrichment, $F_{\gamma_1}$ and $F_{\gamma_2}$, and a corresponding degree of freedom, $\kappa_1$ or $\kappa_2$. Because the non-linear elastic regime is usually restricted to a very small radius around the core, the core enrichment is initially only applied to the element that contains the tip, henceforth called the core element. So the weak and strong nodes are still applied to all nodes on the glide plane, but the core enrichment only to the core elements. The complete DCE-FEM formulation then becomes

$$\boldsymbol{u}^h(\boldsymbol{x}) = \sum_{i\in I_h} \varphi_i(\boldsymbol{x})\boldsymbol{u}_i + \sum_{\gamma=0}^{n_D}\left(\sum_{i\in I_w^{\gamma}} \psi_i(\boldsymbol{x})\boldsymbol{\alpha}_i + \sum_{i\in I_s^{\gamma}} \chi_i(\boldsymbol{x})\boldsymbol{b}^{\gamma} + \boldsymbol{F}_{\gamma 1}(\boldsymbol{x})\kappa_{\gamma 1} + \boldsymbol{F}_{\gamma 2}(\boldsymbol{x})\kappa_{\gamma 2}\right). \tag{4.2}$$

In this formulation, the Kronecker property is no longer conserved at the nodes within the core, because it has non-zero values at the edges of the element. This causes parasitic terms and errors in the blending elements between the core end the rest of the mesh. Also, the jump at the edge of the core element is prescribed twice. To solve this, the core enrichment is shifted by subtracting the linear DE-FEM solution, yielding a purely non-linear function. This core enrichment is 0 at the element boundaries and it has no jump at the edge anymore. It is plotted in Figure 4.3 and contains only the non-linear part of the singularity, because the linear parts of each integration element are subtracted. This is added to the core enrichment function to be

$$\boldsymbol{F}_{\gamma\lambda}(\boldsymbol{x}) = \boldsymbol{f}^{\gamma\lambda}_{\text{exact}}(\boldsymbol{x}) - \left(\sum_{i\in I^{\gamma\lambda}_{\text{core}}} \varphi_i(\boldsymbol{x})\boldsymbol{u}_i + \sum_{i\in I^{\gamma\lambda}_{w,\text{core}}} \psi_i(\boldsymbol{x})\boldsymbol{\alpha}_i + \sum_{i\in I^{\gamma\lambda}_{s,\text{core}}} \chi_i(\boldsymbol{x})\boldsymbol{b}\right). \tag{4.3}$$

Unfortunately, by subtracting the linear DE-FEM part, the core enrichment now depends on some of the standard and other enriched degrees of freedom as well. This is a big problem, because non-linear cross-terms like $\boldsymbol{u}_i\boldsymbol{\kappa}_{\gamma 1}$ and $\boldsymbol{\alpha}_i\boldsymbol{\kappa}_{\gamma 1}$ are introduced to the linear system of equations. Since this was deemed to be beyond the scope of this thesis, a quick-fix solution was created by approximating the DE-FEM solution without core enrichment, and to subtract this piece-wise linear displacement field, before computing the singular

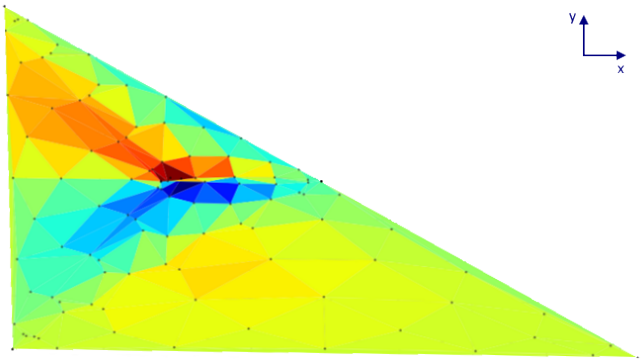


Figure 4.3: Sketch of the horizontal displacement of the purely non-linear core enrichment over a triangular element. It is constructed as the exact analytical solution over the core triangular element that contains the tip minus the linear DE-FEM part of that same element. The element contains no jump at the edge, but only at the tip, creating a singularity. Red indicates a positive and blue a negative displacement in the $x$-direction.

stiffness of the enrichment and solving the system. Although this is a rough approximation, it could at least demonstrate the applicability of the shifted core enrichment.

### 4.2.2. SINGULAR QUADRATURE

To evaluate the singular enrichment, an adapted quadrature method is used, *i.e.*, a mapping method introduced by Nagarajan and Mukherjee [39]. It consists of several steps and is shortly summarized below. First the global coordinates, $\boldsymbol{x}$, are transformed to local triangle, $\bar{\boldsymbol{\xi}}$, via the isoparametric mapping. Then from this master triangle ($[0,0],[1,0],[0,1]$) the coordinates are transformed to a square $(\bar{\rho},\bar{\theta})$ with $\rho$ from $[0,1]$ and $\theta$ from $[0,\frac{\pi}{2}]$ by the inverse of the following transformation:

$$T_M : (\bar{\rho},\bar{\theta}) \longmapsto (\bar{\xi},\bar{\eta}) \tag{4.4}$$

where

$$\bar{\xi} = \bar{\rho}\cdot\cos^2\bar{\theta}, \qquad \bar{\eta} = \bar{\rho}\cdot\sin^2\bar{\theta}. \tag{4.5}$$

The mapping of this transformation is given by the Jacobian

$$J_M = \bar{\rho}\cdot\sin\left(2\bar{\theta}\right). \tag{4.6}$$

Finally the square is scaled back to a simple $[-1,1]\times[-1,1]$ rectangle, which is evaluated using normal Gaussian quadrature. Because of the Jacobian's direct dependence on the radius ($\rho$), the $1/r$ singularity is eliminated from the integrand. The final integration for the singular enrichment is then computed by evaluating at the gauss points for a rectangle, and transforming it back to the global triangle, *i.e.*,

$$\int_\Omega \tilde{f}(\boldsymbol{x})\,\mathrm{d}\Omega = \sum_i^n\sum_j^n \tilde{f}(\xi_i,\eta_j)J_\xi J_M(\xi_i,\eta_j)J_q w_i w_j \tag{4.7}$$

where $\Omega$ is the domain over which the singular function $\tilde{f}$ is integrated, $J_\xi$ is the normal Jacobian associated with the isoparametric mapping from global to local coordinates, $J_M$ is the above described transformation, which depends on the local coordinates, and $J_q$, the Jacobian of the scaling of the rectangle, which is constant $(\pi/8)$.

### 4.2.3. RESULTS

First, the evaluation of the singular enrichment by the adaptive quadrature was verified, by checking the measure of the core element and discovering the number of Gauss points required. For a single dislocation, on a 31x31 mesh, the error in the $\mathscr{L}^2$ norm and associated weight, $\kappa_{\gamma 1}$, are plotted against the number of Gauss points in Figure 4.4 and 4.5. It can be seen, that for the singular quadrature the core enrichment is evaluated properly, as opposed to the normal quadrature. The error in the $\mathscr{L}^2$ norm is increasing with the number of Gauss points. A lot of Gauss points are required for the error to converge. This is in line with the findings of Park [40].

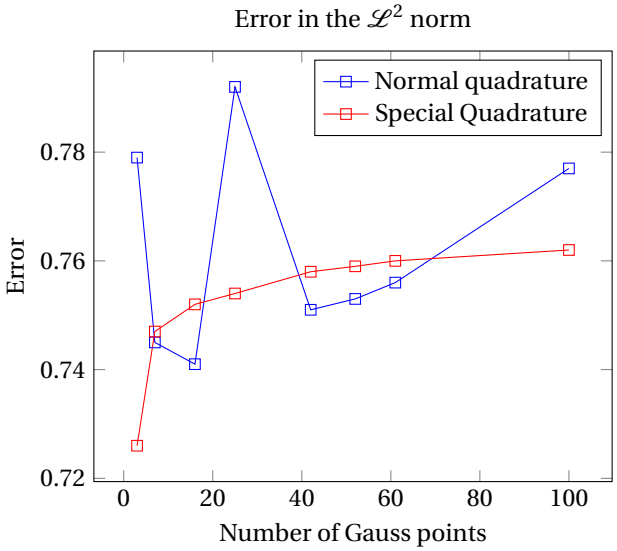


Figure 4.4: The $\mathscr{L}^2$-error norm for increasing number of Gauss points to evaluate the core for normal, and the special, singular quadrature

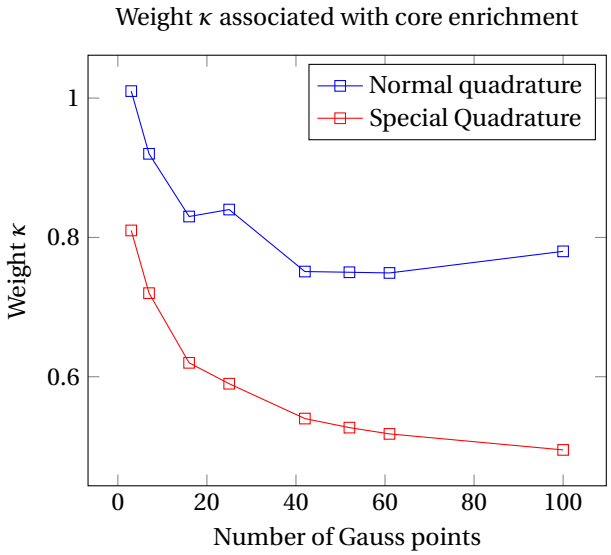


Figure 4.5: The associated weight, $\kappa_{\gamma 1}$, for increasing number of Gauss points for normal, and singular quadrature

For a single dislocation in the center of a 2 µm × 2 µm domain, with 31x31 elements the error in the $\mathscr{L}^2$ norm is computed. Without core enrichment it is 0.010, with core enrichment it is 0.0076. If the core enrichment is not shifted, it is even worse: 0.015. The improved accuracy of the shifted core enrichment demonstrates that it works, although the effect is still not optimal because the enrichment is limited to one element. An extension to multiple elements is cumbersome though, as long as the enrichment depends on standard dofs. Because computing the enrichment over the entire mesh is highly undesirable, it should only be applied locally and extra care needs to be taken for the blending elements around each dislocation. As for the Peach-Köhler stress computation, the enriched dofs and the core enrichment are neglected, but the remaining stress field does not converge to the desired Peach-Köhler stress. Also retrieval of the non-enriched surrounding elements does not work, because the stresses keep increasing with mesh refinement due to the limited range of the enrichment. Hence, it needs to be defined over multiple elements and independent with the mesh size. One approach to do so, would be to built it upon the partition of unity, as is already done in X/GFEM. Then boundary conditions are taken care of by the partition of unity, but the advantages of DE-FEM over X/GFEM are lost again. This, and due to the non-linear cross-terms introduced in the formulation and the required computational cost of the singular core enrichment, led to the conclusion that DCE-FEM is an unviable alternative for existing discrete dislocation simulations for this thesis. For further research, a possible continuation would lie in the extension of the enrichment over multiple elements to a mesh independent domain, while still being built on these elements for simple boundary condition application. Also preferably an alternative for the singular quadrature is used to numerically integrate the enrichment, like converting the enrichment to a contour integral for example.

## 4.3. AN ALTERNATIVE APPROACH

This alternative approach is an attempt to model discrete dislocation dynamics with DE-FEM, where each dipole field is computed separately. Even though it is computationally inefficient for a small number of dislocations, it might be an attractive method for a large number of dislocation, because it tries to decrease the order of complexity for the Peach-Köhler force computations below $\mathcal{O}(n_d^2)$, with $n_d$ the number of dislocations. In an attempt to decrease the computational effort, a static condensation approach is implemented. This section explains the formulation of this alternative approach, it shortly recaps the applied concept of static condensation and it shows the results for the error and the computation of the Peach-Köhler forces.

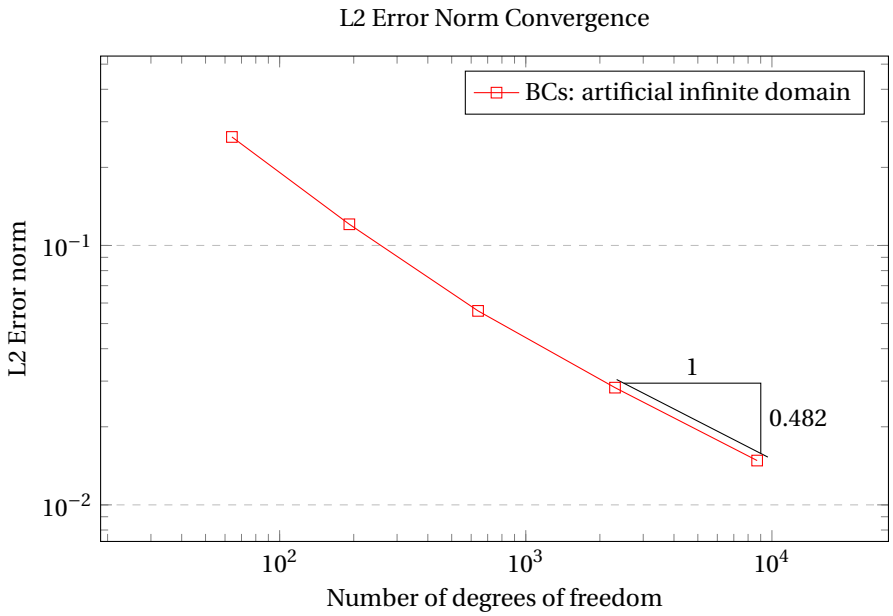


Figure 4.6: Convergence of the superposition of all separate dipole fields to the combined stationary solution for an artificial infinite domain.

### 4.3.1. FORMULATION

The general idea is to apply the superposition principle by Van der Giessen and Needleman [7] to DE-FEM fields. So a field with two dipoles (*i.e.*, four dislocations) is decomposed in three fields: one field for each dipole (two fields, four dislocations) and one normal FEM field that contains all the applied boundary conditions. Since the numerical fields are all linear they can be added together to yield the total field, such that

$$\boldsymbol{\sigma} = \sum_{i=1}^{n_{dp}} \check{\boldsymbol{\sigma}}_i + \hat{\boldsymbol{\sigma}}, \qquad \boldsymbol{\epsilon} = \sum_{i=1}^{n_{dp}} \check{\boldsymbol{\epsilon}}_i + \hat{\boldsymbol{\epsilon}}, \qquad \boldsymbol{u} = \sum_{i=1}^{n_{dp}} \check{\boldsymbol{u}}_i + \hat{\boldsymbol{u}} \tag{4.8}$$

where the $\check{\cdot}_i$ field is the DE-FEM computed field for the $n_{dp}$ dipoles with zero boundary conditions applied to the global boundary $\Gamma$, *i.e.*, $\check{\boldsymbol{u}} = \boldsymbol{0}$ on $\Gamma_u$ and $\check{\boldsymbol{T}} = \boldsymbol{0}$ on $\Gamma_f$ and $\Gamma = \Gamma_u \cup \Gamma_f$. $\hat{\boldsymbol{u}}$ is a smooth, linear field, without any dipoles or discontinuities, but with only the actual boundary conditions applied ($\hat{\boldsymbol{u}} = \boldsymbol{u}_0$ on $\Gamma_u$ and $\hat{\boldsymbol{T}} = \boldsymbol{T}_0$ on $\Gamma_f$).

Apart from a small computational error introduced by the extra computation steps, it can be demonstrated that this "superposed" DE-FEM solution quickly converges to the exact solution. This is shown by the convergence rate of the error in the $\mathscr{L}^2$ norm, computed for a "boundaryless" numerical field, *i.e*, the global applied boundary conditions mimic an infinite space, and shown in Figure 4.6. When boundary conditions are imposed, it can be compared with the superposition method of Van der Giessen and Needleman [7] and shown to converge to the same field as well, proving the accuracy of this DE-FEM superposition approach.

### 4.3.2. STATIC CONDENSATION

In order to reduce the computational cost, a static condensation method is used. Normally a FEM computation solves the linear system

$$\boldsymbol{KU} = \boldsymbol{F} \tag{4.9}$$

where $\boldsymbol{K}$ is the stiffness matrix, $\boldsymbol{F}$ the force vector and $\boldsymbol{U}$ the nodal degrees of freedom. Most of the computation time lies in solving the global system, $\boldsymbol{K}^{-1}\boldsymbol{F}$. Because this superposition approach recomputes the same field every time, but for a different dipole, the static condensation makes sure that the stiffness of all elements untouched by any discontinuity are reused for each computation. This is done by decomposing the total stiffness matrix as

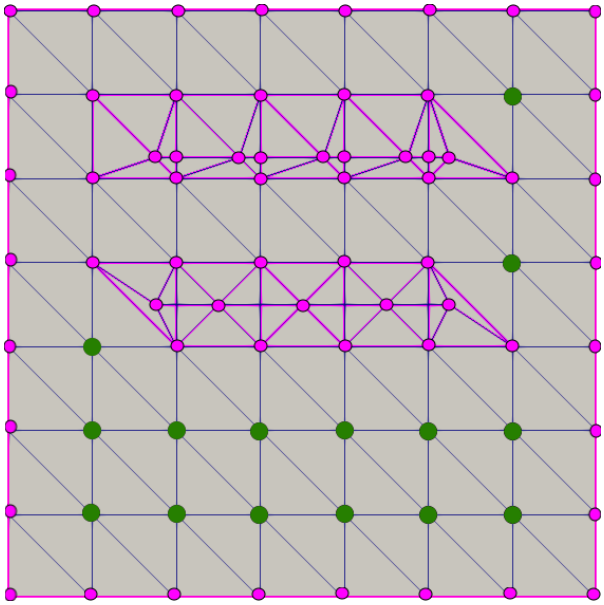

Figure 4.7: The nodes connected to an enriched element or a boundary are pink, and they are directly influenced to the prescribed dipole boundary conditions. The remaining nodes are green, and considered to be free.

$$\begin{bmatrix} \boldsymbol{K_{ff}} & \boldsymbol{K_{fp}} \\ \boldsymbol{K_{pf}} & \boldsymbol{K_{pp}} \end{bmatrix} \begin{Bmatrix} \boldsymbol{u_f} \\ \boldsymbol{u_p} \end{Bmatrix} = \begin{Bmatrix} \boldsymbol{f_f} \\ \boldsymbol{f_p} \end{Bmatrix} \tag{4.10}$$

where $\boldsymbol{u_f}$ denotes the free nodes, and $\boldsymbol{u_p}$ the prescribed nodes. The prescribed nodes consist of the combined set of all enriched nodes (see Equation 3.1), all the boundary nodes and all the nodes that are connected to an enriched element, *i.e.*, all the standard nodes that are influenced by boundary conditions somewhere in the computation. Figure 4.7 shows in pink the boundary and the enriched elements, whose nodes are prescribed by a dipole. All other nodes are represented by the green dots. They are free and remain unchanged throughout each time step. This means that $\boldsymbol{K_{ff}}$ and its inverse $\boldsymbol{K_{ff}^{-1}}$ only have to be computed once. The free nodes $\boldsymbol{u_f}$ can then be written as a function of the prescribed nodes $\boldsymbol{u_p}$ as

$$\boldsymbol{u_f} = \boldsymbol{K_{ff}^{-1}} \left( \boldsymbol{f_f} - \boldsymbol{K_{fp}} \boldsymbol{u_p} \right) \tag{4.11}$$

where $\boldsymbol{f_f} = \boldsymbol{0}$, because they are free from external stress. The formula for the prescribed nodes can be deduced following the same logic, where the dependence on the free nodes $\boldsymbol{u_f}$ is removed:

$$\boldsymbol{K_{pp}} \boldsymbol{u_p} + \boldsymbol{K_{pf}} \boldsymbol{u_f} = \boldsymbol{f_p} = \left( \boldsymbol{K_{pp}} - \boldsymbol{K_{pf}} \boldsymbol{K_{ff}^{-1}} \boldsymbol{K_{fp}} \right) \boldsymbol{u_p} = \boldsymbol{K'} \boldsymbol{u_p}. \tag{4.12}$$

The adapted stiffness matrix $\boldsymbol{K'}$ needs to be computed and inverted for every dipole field, but as the meshes refine, the relative number of free nodes increases, which yields considerable savings in computation time. The retrieval of the free nodes $\boldsymbol{u_f}$ is straightforward when $\boldsymbol{u_p}$ is known:

$$\boldsymbol{u_f} = -\boldsymbol{K_{ff}^{-1}} \boldsymbol{K_{fp}} \boldsymbol{u_p} = \boldsymbol{K''} \boldsymbol{u_p} \tag{4.13}$$

### 4.3.3. PEACH-KÖHLER FORCE

The DE-FEM superposition approach is explicitly designed to separate the self-stress from the total stress and to compute the configurational Peach-Köhler stress. It makes use of the fact, that the accuracy of the numerical stress field around a dislocation (without any core enrichment, but with only the Burgers vector prescribed over the glide plane) increases further away from the singularities. For dislocation $\gamma$, the Peach-Köhler stress $\boldsymbol{\sigma}_{PK}^{\gamma}$ can be retrieved by subtracting its dipole stress field from the total stress field. Because both fields have identical integration elements and the strains due to the dislocation increase similarly with mesh refinement, the numerical singularity can now be removed and the stress due to the boundary conditions and other dislocations remains. So the Peach-Köhler stress for dislocation $\gamma$ at coordinate $X^{\gamma}$ can be written mathematically, similarly to the original Peach-Köhler equation (Equation 2.13), as

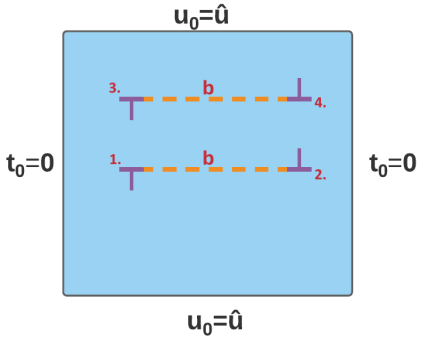


Figure 4.8: A simple problem with 4 dislocations inside a 2 µm × 2 µm domain, with the left and right boundary traction-free, and a displacement offset at the top and bottom boundary.

$$\boldsymbol{\sigma}^{\gamma}_{PK} = \hat{\boldsymbol{\sigma}}(\boldsymbol{x}^{\gamma}) + \sum_{j \neq \gamma}^{n_{dp}} \check{\boldsymbol{\sigma}}^{j}(\boldsymbol{x}^{\gamma}) \tag{4.14}$$

where $n_{dp}$ is the number of dipoles in the problem and $j \neq \gamma$ refers to all dipoles except the one which contains dislocation $\gamma$. $\hat{\boldsymbol{\sigma}}$ refers to the smooth FEM field with the applied boundary conditions, and $\check{\boldsymbol{\sigma}}^{j}$ to the DE-FEM field for dipole $j$.

### EXTRA CONTRIBUTIONS

For an accurate Peach-Köhler stress value, two extra contributions have to be included. One is the value of the other dislocation of the same dipole (its "brother"), which is excluded along with the entire dipole. In an infinite domain this is easily computed. The least squares fit can be used as well, and a numerical solution for a single dislocation also exists, as was shown in Section 3.5.2, but this does require the computation of an extra DE-FEM field.

The other contribution comes from the image field, compensating for the presence of the dislocation itself. This is best illustrated for a single dislocation in a fully clamped field, *i.e.*, $\hat{\boldsymbol{u}} = \boldsymbol{0}$ on $\Gamma_u$. Even though no external stresses are applied on the domain, there are internal stresses due to the dislocation. The superposition approach by Van der Giessen [7] suggests that by constructing an image solution to counter the dislocation stresses at the boundary, the stresses due to this image acting on the dislocation are non-zero as well, *i.e.*, the effect of the configurational stress on itself via the boundaries. Only if a dislocation is far away from any boundary this contribution can be neglected, but since the dislocation stress has a $1/r$ singularity, it has a long range stress field and the image field needs to be considered.

### PEACH-KÖHLER SUPERPOSITION

The entire calculation procedure is depicted schematically in Figure 4.9 for a problem with two dipoles and a shear displacement at top and bottom, as shown in Figure 4.8. The procedure shows two different parts. The first part, concerning the blue fields, contains the summation of all separate dipole fields plus a different FEM field for the applied boundary conditions. This superposition amounts to the stationary solution of all dislocations, as put in Equation 4.8. Field (1) is the normal FEM field which computes the effect of the globally applied boundary conditions at each point. Field (2) is a DE-FEM field with the effects of the first dipole incorporated (*i.e.*, the glide plane enrichment) and with the boundary conditions chosen as clamped and traction-free, such that superposing it to field (1) does not influence the originally applied boundary conditions. Field (3) is the equivalent to field (2), but for the other dipole.

The second part is about the extra contributions needed to accurately compute the Peach-Köhler stress for a certain dislocation: one for the other dislocation of the same dipole and one for the image field. The green fields and the yellow fields denote two different approaches for these extra contributions. To illustrate the procedure the Peach-Köhler stress for the right bottom dislocation is computed and its location depicted with a yellow diamond. At each numerical field the stress needs to be interpolated at those coordinates. First of all all the yellow diamonds from the blue fields are to be added together *or* the stress field of the bottom

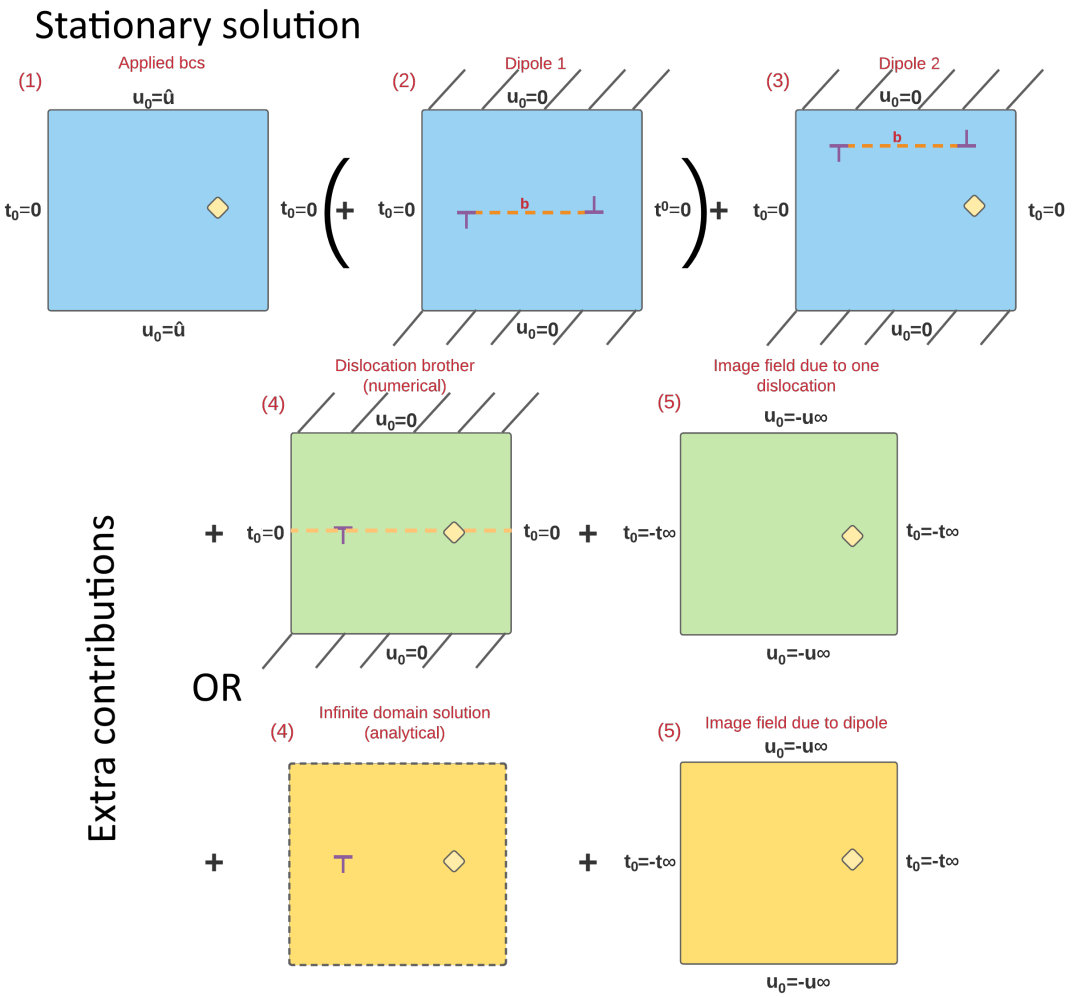


Figure 4.9: Schematic representation of the Peach-Köhler stress computation for the right bottom dislocation using the DE-FEM superposition procedure for a bounded domain with two dipoles. Field 1 is a smooth field which handles all applied boundary conditions, field 2 and 3 are DE-FEM fields for the first and second dipole, respectively. Summation of fields 1-3 yields the total displacement field and contains all singularities. For computing the Peach-Köhler force, the numerical stress field of the dipole of concern needs to be subtracted. For the Peach-Köhler force computation two different approaches are sketched in 4 and 5. For the green fields, field 4 is a DE-FEM field with a single dislocation and field 5 is a smooth image field. For the yellow fields the superposition principle is used, with field 4 the analytical infinite domain, and field 5 the image solution. The yellow diamond shows the place of the dislocation where the stresses need to be calculated.

dipole is to be subtracted from the total stress. That is why the second blue field in Figure 4.9 is between brackets. Next, the extra contributions are included.

The first approach for these contributions, denoted by the green fields, is to compute the stress due to the other dislocation numerically using DE-FEM, as demonstrated in Section 3.5.2, and shown in field (4). The image field (5) then only needs to account for the image stress due the omitted dislocation, *i.e.*, the right bottom dislocation. The boundary conditions of the image field are the inverse tractions and displacements that would rise at the boundaries due to infinite solution of this one dislocation.

Alternatively for the second approach, the yellow fields show a compromise with the original superposition principle. Field (4) is now the analytical solution from either the fit or the exact infinite domain, and the image field (5) is now computed based on the boundary conditions created by both dislocations, *i.e.*, the dipole. This has the advantage that the image field needs only be computed once per dipole (instead of once per dislocation). An extra option is to replace the analytical solution by the numerical fit, as found in Section 3.5.2, but the analytical solution is probably more accurate. So to summarize, for the case of the right dislocation of the bottom dipole, located at $\boldsymbol{x} = (1.5, 1.0)$, the contributions for the Peach-Köhler stress come from the background field 1, the stresses of the upper dipole in field 3, the contribution of the other dislocation of the same dipole 4 and the image stress due to itself, field 5. Field 2 is excluded because it has a numerical

Table 4.1: The table above shows the numerical Peach-Köhler stresses in MPa for the DE-FEM superposition approach of the different fields depicted in Figure 4.9, converging with mesh refinement, of the bottom-right dislocation (located at $\boldsymbol{x}$=(1.5,1.0)) from the problem in Figure 4.8. Note the three different ways to compute field 4: a) uses the numerical DE-FEM values, b) uses the exact analytical relations and c) uses the least squares fit. Hence 4b) is the same as the analytical value from field 4 in the original superposition method. Because the total stress values using 4c) were worse, than 4b) they are omitted from this table. The table below shows the same Peach-Köhler stress values, but for the original superposition method. Note that only the background field converges over time as the analytical infinite domain stresses are exact and mesh independent.

DE-FEM Superposition

| | 1) | | | 3) | | | 4a) | | | 4c) *(fit)* | | |
|---|---|---|---|---|---|---|---|---|---|---|---|---|
| $n_{\text{elemx}}$ | $\sigma_{11}$ | $\sigma_{22}$ | $\sigma_{12}$ | $\sigma_{11}$ | $\sigma_{22}$ | $\sigma_{12}$ | $\sigma_{11}$ | $\sigma_{22}$ | $\sigma_{12}$ | $\sigma_{11}$ | $\sigma_{22}$ | $\sigma_{12}$ |
| 15 | 0.36 | 0.16 | 20.90 | 0.43 | 2.70 | -1.55 | -0.02 | -0.01 | -1.86 | -0.02 | 0.06 | -1.38 |
| 31 | 0.11 | 0.08 | 20.76 | 0.03 | 2.75 | -1.73 | -0.01 | -0.01 | -1.86 | -0.02 | 0.05 | -1.42 |
| 63 | 0.04 | 0.04 | 20.69 | -0.03 | 2.74 | -1.70 | 0.00 | 0.00 | -1.86 | -0.01 | 0.04 | -1.45 |
| 127 | 0.01 | 0.02 | 20.67 | -0.05 | 2.72 | -1.72 | 0.00 | 0.00 | -1.86 | -0.01 | 0.03 | -1.47 |

| | 5a) | | | 5b) | | | Total a) | | | Total b) | | |
|---|---|---|---|---|---|---|---|---|---|---|---|---|
| $n_{\text{elemx}}$ | $\sigma_{11}$ | $\sigma_{22}$ | $\sigma_{12}$ | $\sigma_{11}$ | $\sigma_{22}$ | $\sigma_{12}$ | $\sigma_{11}$ | $\sigma_{22}$ | $\sigma_{12}$ | $\sigma_{11}$ | $\sigma_{22}$ | $\sigma_{12}$ |
| 15 | -0.14 | 0.00 | 0.56 | -0.14 | 0.00 | 0.26 | 0.63 | 2.83 | 18.06 | 0.65 | 2.86 | 18.05 |
| 31 | -0.06 | -0.01 | 0.68 | -0.05 | -0.01 | 0.38 | 0.10 | 2.81 | 17.84 | 0.09 | 2.82 | 17.85 |
| 63 | -0.02 | 0.00 | 0.71 | 0.02 | 0.00 | 0.41 | -0.02 | 2.77 | 17.84 | 0.03 | 2.78 | 17.84 |
| 127 | -0.01 | -0.02 | 0.72 | 0.04 | 0.00 | 0.43 | -0.05 | 2.73 | 17.80 | 0.00 | 2.74 | 17.82 |

Original Superposition

| | 1+5) *(image)* | | | 3) *(analytical)* | | | 4) *(analytical)* | | | Total) | | |
|---|---|---|---|---|---|---|---|---|---|---|---|---|
| $n_{\text{elemx}}$ | $\sigma_{11}$ | $\sigma_{22}$ | $\sigma_{12}$ | $\sigma_{11}$ | $\sigma_{22}$ | $\sigma_{12}$ | $\sigma_{11}$ | $\sigma_{22}$ | $\sigma_{12}$ | $\sigma_{11}$ | $\sigma_{22}$ | $\sigma_{12}$ |
| 15 | -1.04 | -0.56 | 20.21 | 1.36 | 3.37 | -0.71 | 0.00 | 0.00 | -1.56 | 0.32 | 2.81 | 17.94 |
| 31 | -1.31 | -0.60 | 20.14 | 1.36 | 3.37 | -0.71 | 0.00 | 0.00 | -1.56 | 0.04 | 2.78 | 17.86 |
| 63 | -1.39 | -0.63 | 20.10 | 1.36 | 3.37 | -0.71 | 0.00 | 0.00 | -1.56 | -0.03 | 2.74 | 17.83 |
| 127 | -1.41 | -0.65 | 20.08 | 1.36 | 3.37 | -0.71 | 0.00 | 0.00 | -1.56 | -0.05 | 2.73 | 17.81 |

singularity at the dislocation coordinate.

### 4.3.4. RESULTS

The method was tested on a 2 µm × 2 µm domain for the problem with two dipoles as shown in Figure 4.8, a Young's modulus $E$ =70 GPa and a Poisson's ratio $\nu = 0.33$. The boundary conditions are chosen traction-free at the sides, and a shear displacement offset at the top and bottom of 1 nm, such that

$$\boldsymbol{u}^0 = \begin{bmatrix} 0.001 \\ 0 \end{bmatrix} \qquad \text{at } \Gamma_{u,\text{top}}, \tag{4.15}$$

$$\boldsymbol{u}^0 = \begin{bmatrix} -0.001 \\ 0 \end{bmatrix} \qquad \text{at } \Gamma_{u,\text{bottom}}, \tag{4.16}$$

with $\boldsymbol{u}$ given in µm, yielding a global shear strain $\gamma_{12}$ of 0.001.

To verify the Peach-Köhler stress, the values for one dislocation are compared to the analytical solution with mesh refinement. The stresses are computed for a mesh with 15×15, 31×31, 63×63 and 127×127 triangular elements. The results of each step of the computation of the Peach-Köhler stress are shown in Table 4.1 for the bottom-right dislocation at $\boldsymbol{x} = (1.5, 1)$. Hence the computational scheme from Figure 4.9 can be followed. The Peach-Köhler stress follows from the summation of the yellow diamond values in fields (1), (3), (4) and (5). They are compared with the superposition of the analytical infinite domain fields and the image field, as proposed by Van der Giessen [7], and will be referred to as the analytical solution. Note that the individual fields have different boundary conditions, so only the final value can be compared directly.

The total stress values from the table are plotted in Figures 4.10 - 4.12. They show that the Peach-Köhler stress tends to the analytical solution with mesh refinement. Both approaches to include the stress of the

other dislocation of the same dipole and the image stress, as discussed before and depicted in the green and yellow fields in Figure 4.9 are accurate. The least squares fit, or field 4c) as it is referred to in Table 4.1, is not used because it is significantly less accurate. This makes a lot of sense, because the fit approaches the exact infinite domain solution with mesh refinement, but it will of course never be as accurate as the exact infinite domain solution. Therefore its use is omitted from the total stress calculations and the simulations in the next section.

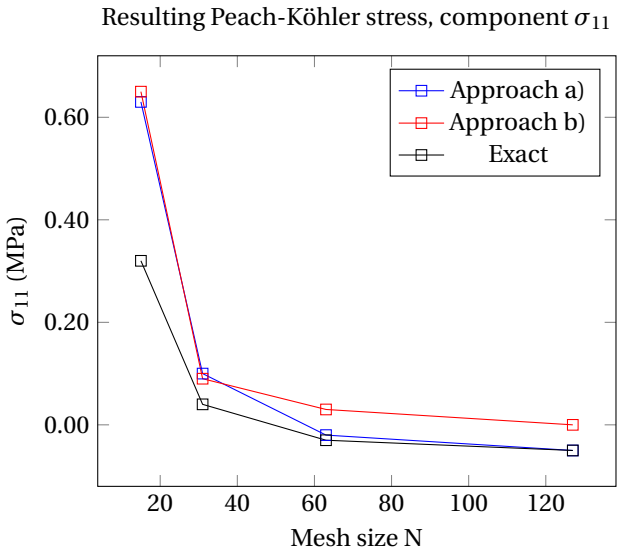


Figure 4.10: Total Peach-Köhler stress values for $\sigma_{11}$ with mesh refinement. For the extra contributions of the image stress and the other dislocation two different approaches are plotted. Approach a) computes the numerical DE-FEM field for the dislocation brother, and the image field for the dislocation itself. Approach b) uses the exact analytical values and the image field for both the dislocation itself and its brother.

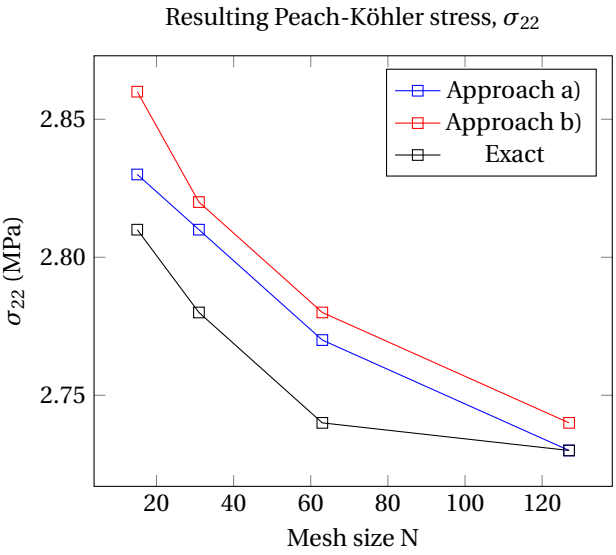


Figure 4.11: Total Peach-Köhler stress values for $\sigma_{22}$ with mesh refinement. For the extra contributions of the image stress and the other dislocation two different approaches are plotted. Approach a) computes the numerical DE-FEM field for the dislocation brother, and the image field for the dislocation itself. Approach b) uses the exact analytical values and the image field for both the dislocation itself and its brother.

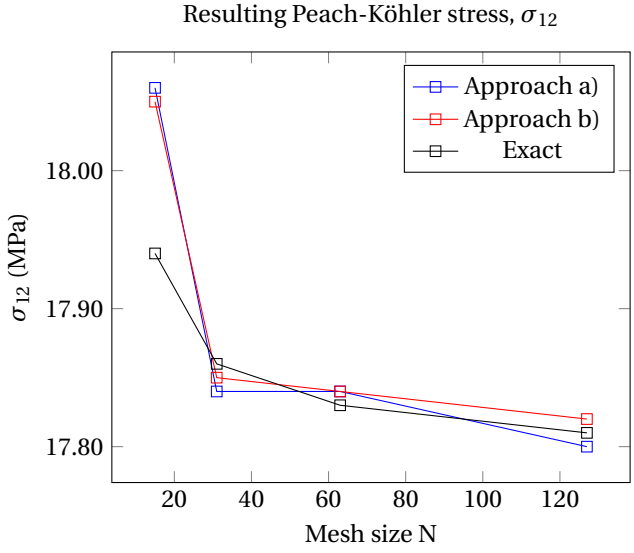


Figure 4.12: Total Peach-Köhler stress values for $\sigma_{12}$ with mesh refinement. For the extra contributions of the image stress and the other dislocation two different approaches are plotted. Approach a) computes the numerical DE-FEM field for the dislocation brother, and the image field for the dislocation itself. Approach b) uses the exact analytical values and the image field for both the dislocation itself and its brother.

Table 4.2: The initial dislocation positions at t=0 ns and its final locations. Because dislocation 5-8 are annihilated after 12 ns, the values for t=10 ns are shown as well.

| Dislocation | 1 | | 2 | | 3 | | 4 | |
|---|---|---|---|---|---|---|---|---|
| | x | y | x | y | x | y | x | y |
| $t_0$ | 1.20 | 0.80 | 1.40 | 0.80 | 1.20 | 0.50 | 1.40 | 0.50 |
| $t_{15}$ - Analytical | 0.372 | 0.80 | 1.887 | 0.80 | 0.382 | 0.50 | 1.916 | 0.50 |
| $t_{15}$ - DE-FEM | 0.375 | 0.80 | 1.888 | 0.80 | 0.384 | 0.50 | 1.916 | 0.50 |
| | 5 | | 6 | | 7 | | 8 | |
| | x | y | x | y | x | y | x | y |
| $t_0$ | 0.25 | 0.867 | 0.75 | 1.733 | 0.45 | 0.867 | 0.95 | 1.733 |
| $t_{10}$ - Analytical | 0.427 | 1.173 | 0.559 | 1.402 | 0.632 | 1.182 | 0.719 | 1.334 |
| $t_{10}$ - DE-FEM | 0.425 | 1.170 | 0.561 | 1.407 | 0.628 | 1.176 | 0.720 | 1.333 |
| $t_{15}$ - Analytical | - | - | - | - | - | - | - | - |
| $t_{15}$ - DE-FEM | - | - | - | - | - | - | - | - |

### 4.3.5. A DISCRETE DISLOCATION DYNAMICS SIMULATION

The DE-FEM superposition approach for simulating discrete dislocation dynamics is compared with the analytical simulation over 36 time steps of 0.5 ns, which was found to be a good compromise between accuracy and computational time [41, 42]. The material and boundary conditions are taken as before. The initial configuration consists of 8 dislocations, comprising two horizontal and two slanted dipoles at an angle of 60 degrees. The mesh is refined to 63 × 63 triangular elements. The movement of dislocations is governed by the principles from Subsection 2.1.4, *i.e.*, in a quasi-static framework and with the phonon drag as only significant resistance. The phonon drag constant is assumed to be $B = 10^{-4}$ Pa s. An explicit forward Euler scheme is used as simple time stepping algorithm.

The nucleation of new dislocations and the formation of junctions are not incorporated in this model yet, but when two oppositely signed dislocations meet at the same slip plane, they are modelled to annihilate within a distance of 30 nm. This value is an estimate and can be varied. The initial positions of the dislocations, and their numbering, are plotted in Figure 4.14a), the movement over time in Figure 4.14b) and c) and the final positions after $t$=15 ns are given by Table 4.2 and Figure 4.14d). Due to the applied shear force and the dislocation stresses, the slanted dipoles shrink and annihilate at $t$=12 ns, while the horizontal dipoles grow over time and will hit the boundary at $t$=18 ns. The reference solution refers to the superposition method by Van der Giessen and Needleman [7] and is also shown in Figure 4.14d).

The final differences are small and this example demonstrates the overall accuracy for small problems like these. It helps in this case that the motion is limited to glide motion only, because the numerical estimates for the shear stress, which is the driving stress for glide, were very accurate. Hence the discrepancies in the normal stress components are less of an issue. In Figure 4.13 the errors between the superposed DEFEM solution and the reference solution are plotted over time. The numbering in the figure refers to the numbering given in Figure 4.14a). The maximum error occurs in the dislocations of the slanted dipoles, just before they annihilate, at which it has an error of 0.012 µm. Since the slanted dipoles are most affected by the discrepancies in the normal numerical stresses for the Peach-Köhler force computation, this makes a lot of sense. When the slanted dipoles annihilate, the exact are modelled to annihilate as well and the error returns to zero. The other errors keep increasing over time, as would be expected, but the error is significantly smaller. Although this proves the accuracy of this alternative approach, the computation time for this superposed non-optimized DEFEM approach takes about 400 minutes, compared to 5 minutes for the original superposition method, making it 80 times worse in computational performance. The speed of DE-FEM is dependent on implementation and with optimization this time could be significantly reduced to half of that at least and perhaps even more. But in its current form, it is unlikely that this method will prove a viable alternative for modelling discrete dislocation dynamics.

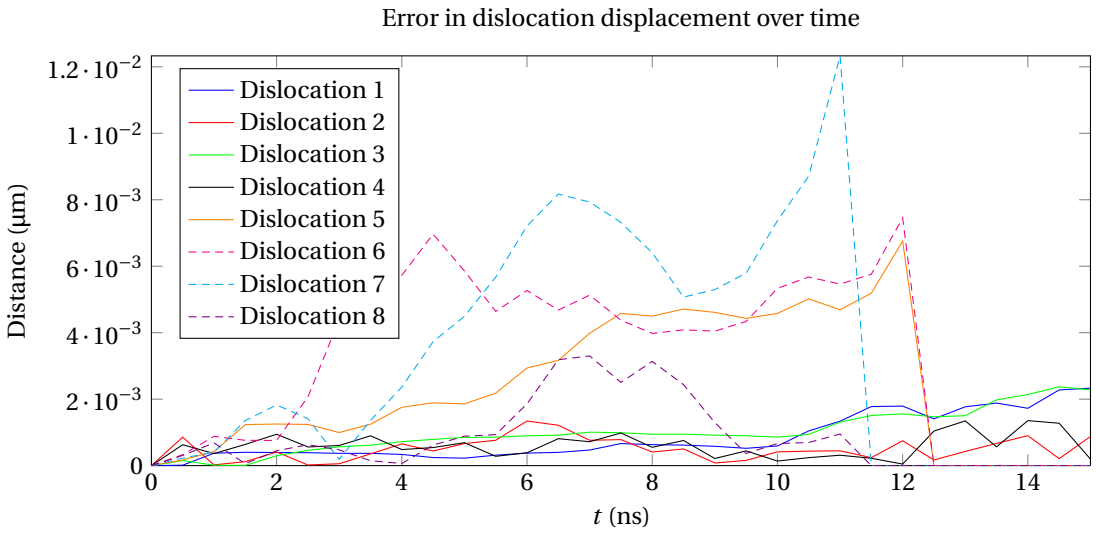


Figure 4.13: Error in the dislocation positions over the first 30 time steps from 0-15 ns. The numbering of dislocations is indicated in Figure 4.14a).

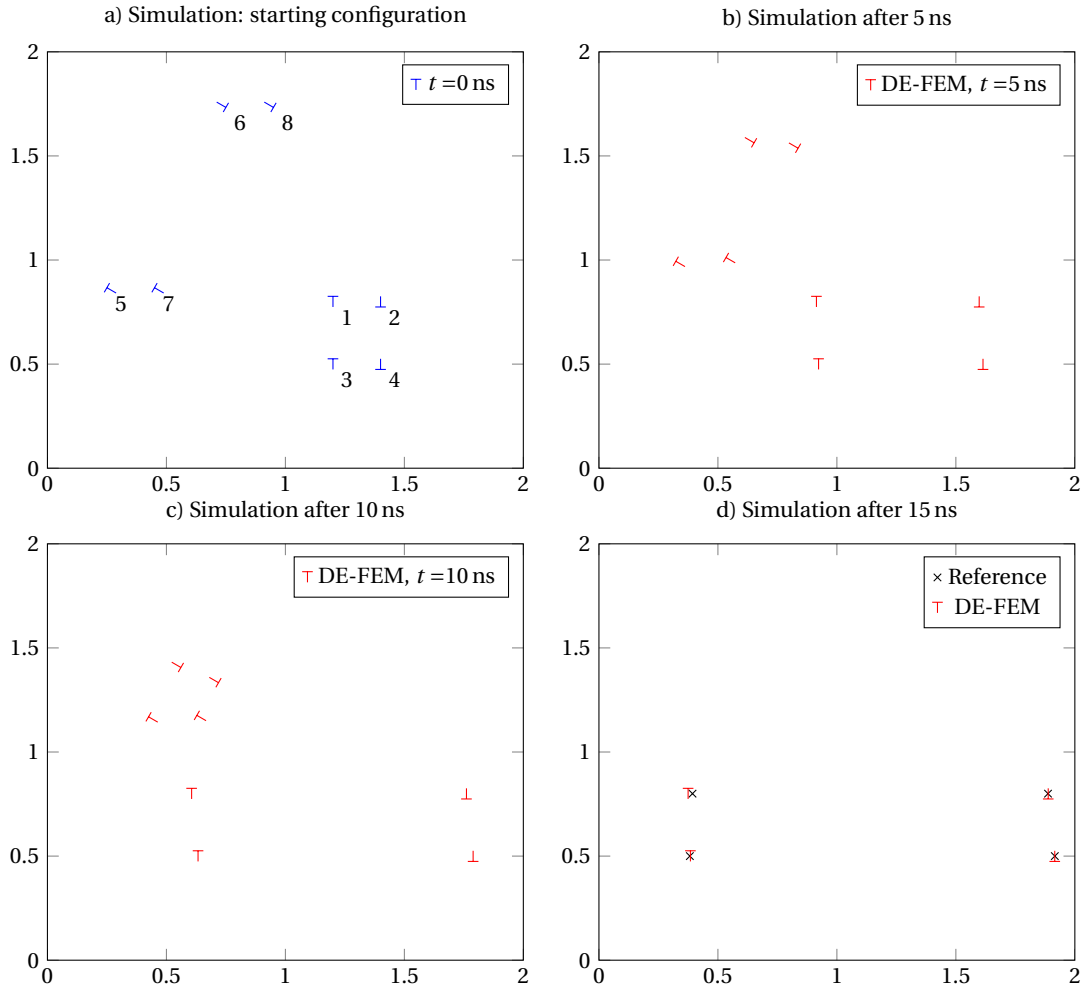


Figure 4.14: The evolution of dislocations in a 2 µm × 2 µm domain over $t$ =15 ns for a under a shear strain of $\gamma_{12} = 0.001$. Figure a) shows the initial positions of the dislocations. In b) and c) the dislocations have glided over their slip plane. Dislocation 5-8 attract each other, while dislocation 1-4 repel. Figure d) shows the final configuration just before the dislocation runs into the boundary. After $t$ =12 ns dislocations 5-8 interact and annihilate, leaving only dislocation 1-4. The reference solution is computed via the superposition principle by Van der Giessen and Needleman [7]

# 5

# CONCLUSIONS

Despite the fact that the current implementation is underperforming in terms of computational time and complexity, there are several conclusions can be drawn from this research. First of all it has been proven and demonstrated that modelling discrete dislocation dynamics with DE-FEM is possible, and for the stationary case very straightforward also. By prescribing a tangential jump over an internal crack, and a weak enrichment at the tips (*i.e.*, the dislocations) to allow the different kinematic fields to merge, the stationary model has shown to have a convergence rate of $\sim 0.5$ in the $\mathscr{L}^2$-norm with respect to the number of degrees of freedom.

The greatest challenge for accurate discrete dislocation dynamics is the correct stress retrieval from the numerical solution and the ability to separate the local stress due to a dislocation from the total stress. Because the stresses are captured with linear elements, a sufficient number is required to accurately capture the stresses. Furthermore, post-processing is necessary to smoothen the field and filter out any jumps for a steady, continuous simulation.

The accurate stress estimation at and around the dislocation cores requires more effort. Because the Burgers vector is a dislocation property, it does not change in magnitude with mesh refinement and the computed strains increase to a numerical singularity. Nearby these numerical stresses are hard to predict with an analytical singular function. Even more so, because within DE-FEM the cut can be placed arbitrarily over an element. While a small change in tip location gives only slightly differently sized integration elements, it can result in large differences in the strains. Even subtracting the analytical solution relatively far away (r=0.2 µm) from around the dislocation, there was still a significant discrepancy in the configurational stress estimate. It is this kind of unpredictability of the numerical core strains, that made subtracting the self-stress from the configurational stress very hard.

To circumvent this problem, an attempt was made to incorporate the singular stresses inside the formulation and let the solver assign a strength to the singularity of each dislocation. Although this approach could work, it does not come without obstacles. Because both core and slip plane are enriched, it is important that the enrichments operate over different domains. Alternatively, the jump over the glide plane needs to be subtracted from the core enrichment, and this subtraction of the jump leads to non-linear cross-terms because the enrichment now depends on some of the degrees of freedom that have yet to be calculated. Another obstacle is the issue of blending elements, since the domain to which the core enrichment is applied needs to be mesh independent and therefore stretch over multiple elements. Finally the evaluation of the singular enrichment requires special quadrature and a lot of Gauss points. Other solution techniques for this integral should be considered. Although an elegant solution combining a singular enrichment with DE-FEM seems far away, there are possibilities to create a viable alternative nonetheless.

Another way to circumvent the problem of separating the self-stress was made by designing a DE-FEM superposition combination. In this approach each dipole field is computed individually using DE-FEM and the superposition of all fields leads to the stationary solution. A static condensation approach is applied to prevent the recomputing of free elements and save computational time. The less elements are intersected by any dislocation, the greater the effect of the static condensation. This DE-FEM superposition is proven

to converge quickly. It is shown that this method allows for the accurate computation of the Peach-Köhler stress, although it should be noted that the numerical estimate for the shear stress component is more accurate than it is for the normal components. Also currently, for each dislocation an extra numerical field and an image field need to be computed, which is very inefficient. This method was used to simulate a 2D discrete dislocation dynamics problem for $t$ =18 ns, with dislocations restricted to glide motion only, and it is shown to be comparable in terms of accuracy to the original superposition method.

As for the computation time however, the current implementation of the alternative approach is much worse than the original superposition method. Although there is plenty of room for optimization, outperforming the original superposition method will be hard, because in this approach, even with the static condensation fully operational, still at least one image field needs to be computed for every dipole (two dislocations), while the original superposition method only requires one FEM field to be computed. For the original Peach-Köhler force computation, the interactions of all $n_d$ dislocations yield a $\mathcal{O}(n_d^2)$ problem, while this is reduced in this approach to $\mathcal{O}(n_d)$. Thus, this approach might prove to be an useful alternative for some specific problems.

# BIBLIOGRAPHY


[1] L. P. Kubin, G. Canova, M. Condat, B. Devincre, V. Pontikis, and Y. Bréchet, *Dislocation Microstructures and Plastic Flow: A 3D Simulation,* Solid State Phenomena **23-24**, 455 (1992).

[2] M. Fivel, *Discrete Dislocation Dynamics: Principles and Recent Applications,* in *Multiscale Modeling of Heterogenous Materials*, edited by O. Cazacu (ISTE, London, UK, 2008) pp. 17–36.

[3] A. Arsenlis, W. Cai, M. Tang, M. Rhee, T. Oppelstrup, G. Hommes, T. G. Pierce, and V. V. Bulatov, *Enabling strain hardening simulations with dislocation dynamics,* Modelling Simul. Mater. Sci. Eng. **15**, 553 (2007).

[4] G. Po, M. S. Mohamed, T. Crosby, C. Erel, A. El-Azab, and N. Ghoniem, *Recent Progress in Discrete Dislocation Dynamics and Its Applications to Micro Plasticity,* JOM **66**, 2108 (2014).

[5] A. Vakis, V. Yastrebov, J. Scheibert, L. Nicola, D. Dini, C. Minfray, A. Almqvist, M. Paggi, S. Lee, G. Limbert, J. Molinari, G. Anciaux, R. Aghababaei, S. Echeverri Restrepo, A. Papangelo, A. Cammarata, P. Nicolini, C. Putignano, G. Carbone, S. Stupkiewicz, J. Lengiewicz, G. Costagliola, F. Bosia, R. Guarino, N. Pugno, M. Müser, and M. Ciavarella, *Modeling and simulation in tribology across scales: An overview,* Tribology International **125**, 169 (2018).

[6] J. P. Hirth and J. Lothe, *Theory of Dislocations*, 2nd ed. (John Wiley & Sons, Inc., 1982).

[7] E. V. der Giessen, E. V. der Giessen, and A. Needleman, *Discrete dislocation plasticity: A simple planar model,* Modelling and Simulation in Materials Science and Engineering **3**, 689 (1995).

[8] N. M. Ghoniem and X. Han, *Dislocation motion in anisotropic multilayer materials,* Philosophical Magazine **85**, 2809 (2005).

[9] G. Ventura, B. Moran, and T. Belytschko, *Dislocations by partition of unity,* International Journal for Numerical Methods in Engineering **62**, 1463 (2005).

[10] I. Babuška and J. M. Melenk, *The Partition of Unity Method,* International Journal for Numerical Methods in Engineering **40**, 727 (1997).

[11] T. Belytschko, N. Moës, S. Usui, and C. Parimi, *Arbitrary discontinuities in finite elements,* International Journal for Numerical Methods in Engineering **50**, 993 (2001).

[12] T. Strouboulis, I. Babuška, and K. Copps, *The design and analysis of the Generalized Finite Element Method,* Computer Methods in Applied Mechanics and Engineering **181**, 43 (2000).

[13] R. Gracie, G. Ventura, and T. Belytschko, *A new fast finite element method for dislocations based on interior discontinuities,* International Journal for Numerical Methods in Engineering **69**, 423 (2007).

[14] R. Gracie, J. Oswald, and T. Belytschko, *On a new extended finite element method for dislocations: Core enrichment and nonlinear formulation73,* Journal of the Mechanics and Physics of Solids **56**, 200 (2007).

[15] R. Gracie, H. Wang, and T. Belytschko, *Blending in the extended finite element method by discontinuous Galerkin and assumed strain methods,* International Journal for Numerical Methods in Engineering (2007).

[16] G. Ventura, R. Gracie, and T. Belytschko, *Fast integration and weight function blending in the extended finite element method,* International Journal for Numerical Methods in Engineering **77**, 1 (2009).

[17] R. Gracie and T. Belytschko, *Concurrently coupled atomistic and XFEM models for dislocations and cracks,* International Journal for Numerical Methods in Engineering **78**, 354 (2009).

[18] J. Oswald, E. Wintersberger, G. Bauer, and T. Belytschko, *A higher-order extended finite element method for dislocation energetics in strained layers and epitaxial islands,* International Journal for Numerical Methods in Engineering **85**, 920 (2011).

[19] A. M. Aragón and A. Simone, *The Discontinuity-Enriched Finite Element Method: The discontinuity-enriched FEM,* International Journal for Numerical Methods in Engineering **112**, 1589 (2017).

[20] T. Belytschko and R. Gracie, *On XFEM applications to dislocations and interfaces,* International Journal of Plasticity **23**, 1721 (2007).

[21] J. Oswald, R. Gracie, R. Khare, and T. Belytschko, *An extended finite element method for dislocations in complex geometries: Thin films and nanotubes,* Computer Methods in Applied Mechanics and Engineering Advances in Simulation-Based Engineering Sciences – Honoring J. Tinsley Oden, **198**, 1872 (2009).

[22] J. Robbins and T. Voth, *Modelling dislocations in a polycrystal using the Generalised Finite Element Method,* IJTAMM **2**, 95 (2011).

[23] S. Liang, Y. Zhu, M. Huang, and Z. Li, *Simulation on crack propagation vs. crack-tip dislocation emission by XFEM-based DDD scheme,* International Journal of Plasticity **114**, 87 (2019).

[24] D. Hull and D. Bacon, *Introduction to Dislocations* (Elsevier, 2011).

[25] G. Yang and S.-J. Park, *Deformation of Single Crystals, Polycrystalline Materials, and Thin Films: A Review,* Materials **12**, 2003 (2019).

[26] V. A. Lubarda, *Dislocation Burgers vector and the Peach–Koehler force: A review,* Journal of Materials Research and Technology **8**, 1550 (2019).

[27] T. Hochrainer, S. Sandfeld, M. Zaiser, and P. Gumbsch, *Continuum dislocation dynamics: Towards a physical theory of crystal plasticity,* Journal of the Mechanics and Physics of Solids **63**, 167 (2014).

[28] H. Cleveringa, E. Van Der Giessen, and A. Needleman, *Comparison of discrete dislocation and continuum plasticity predictions for a composite material,* Acta Materialia **45**, 3163 (1997).

[29] L. K. Wickham, K. W. Schwarz, and J. S. Stölken, *Rules for Forest Interactions between Dislocations,* Phys. Rev. Lett. **83**, 4574 (1999).

[30] T.-P. Fries and T. Belytschko, *The extended/generalized finite element method: An overview of the method and its applications,* International Journal for Numerical Methods in Engineering **84**, 253 (2010).

[31] N. Moës, M. Cloirec, P. Cartraud, and J.-F. Remacle, *A computational approach to handle complex microstructure geometries,* Computer Methods in Applied Mechanics and Engineering **192**, 3163 (2003).

[32] N. Sukumar, D. L. Chopp, N. Moës, and T. Belytschko, *Modeling holes and inclusions by level sets in the extended finite-element method,* Computer Methods in Applied Mechanics and Engineering **190**, 6183 (2001, September 14).

[33] S. Osher and R. P. Fedkiw, *Level Set Methods and Dynamic Implicit Surfaces,* Applied Mathematical Sciences No. v. 153 (Springer, New York, 2003).

[34] G. Ventura and E. Benvenuti, *Equivalent polynomials for quadrature in Heaviside function enriched elements,* International Journal for Numerical Methods in Engineering **102**, 688 (2015).

[35] S. Soghrati, A. M. Aragón, C. A. Duarte, and P. H. Geubelle, *An interface-enriched generalized FEM for problems with discontinuous gradient fields,* International Journal for Numerical Methods in Engineering **89**, 991 (2012).

[36] K. Baxevanakis and A. Giannakopoulos, *Finite element analysis of discrete edge dislocations: Configurational forces and conserved integrals,* International Journal of Solids and Structures **62**, 52 (2015).

[37] R. Gracie and T. Belytschko, *An adaptive concurrent multiscale method for the dynamic simulation of dislocations,* International Journal for Numerical Methods in Engineering **86**, 575 (2011).

[38] D. J. Payen and K.-J. Bathe, *A stress improvement procedure,* Computers & Structures **112-113**, 311 (2012).

[39] A. Nagarajan and S. Mukherjee, *A mapping method for numerical evaluation of two-dimensional integrals with l/r singularity,* Computational Mechanics , 8 (1993).

[40] K. Park, J. P. Pereira, C. A. Duarte, and G. H. Paulino, *Integration of singular enrichment functions in the generalized/extended finite element method for three-dimensional problems,* International Journal for Numerical Methods in Engineering **78**, 1220 (2009).

[41] H. H. M. Cleveringa, E. Van der Giessen, and A. Needleman, *A discrete dislocation analysis of bending,* International Journal of Plasticity **15**, 837 (1999).

[42] C. Ayas, J. A. W. van Dommelen, and V. S. Deshpande, *Climb-enabled discrete dislocation plasticity,* Journal of the Mechanics and Physics of Solids Sixtieth Anniversary Issue in Honor of Professor Rodney Hill, **62**, 113 (2014).

# A

# REFLECTION

The task of modelling discrete dislocation dynamics with DE-FEM is an interesting, but challenging endeavour. DE-FEM has all the advantages of an enriched formulation, such as mesh-independence and it allows for direct prescribing of a discontinuity. But it is not without challenges such as cumbersome implementation and careful post-processing. It was this implementation of DE-FEM in Hybrida, which took a lot of time to get started, even though the code was already there, and I had spent quite some time beforehand on understanding enriched formulations of FEM itself.

But also with the proper understanding of the DE-FEM implementation, another challenge is the correct treatment of the artificial singularities in the field. Although the numerical values are never actually singular, since they are evaluated at Gauss points, they differ in behaviour analytically and numerically. Wrong treatment or slightly wrong assumptions can therefore lead to very unexpected results. It was this unpredictability of the numerical stresses, combined with the requirement for the Peach-Köhler force to exclude the self-stress, which created the real challenge of this project. Our initial assumption that the analytical solution could be subtracted from the numerical stress field did not bear fruit. Because the discontinuity was defined independent of the mesh, integration elements had to be created each time step to evaluate the stiffness of these changing elements. But even minor changes in these integration elements can lead to large differences in the element strain and the numerically computed stresses, creating highly unpredictable core elements. Either many more linear elements were required to accurately capture the stresses, or non-linear elements were needed.

Therefore the core enrichment was another way to incorporate the singularities in the formulation, albeit a very cumbersome method as well. Not only because it is necessary to interface it with Hybrida, and adapted quadrature is required, but also special care needs to be taken for the enriched elements in assembly and post-processing. Because the topological enrichment needs to operate over a fixed range, issues with blending elements arise again and all these steps are very error sensitive. Because this approach required much more work than anticipated, and also takes significant computational time for effective evaluation of the singular function in the stiffness matrix, it was discarded. Even more, it was found that adding the core enrichment only makes sense without affecting the other dofs. If it is applied over the same elements, the measures that need to be taken to prevent this mutual influence, lead to non-linear cross-terms. Therefore, for future research one should try to avoid that by clearly distinguishing between core elements with a singular-like enrichment and slip plane elements with a tangential discontinuity enrichment. Comparison with the purely DE-FEM solution is then no longer possible, because the set of enriched nodes differs slightly. Furthermore, special care is still to be taken for boundary elements with a singular enrichment. In this sense X/GFEM has the advantage, because the core enrichment is then built upon the partition of unity, hence boundaries near the core are computed automatically.

The alternative approach of DE-FEM superposition is invented to find a way to do discrete dislocation simulations with DE-FEM anyway, without subtracting the self-stress of the dislocations. Although it has an interesting approach to lower the order of complexity, it still requires multiple FEM fields to be computed for a single step and the current implementation is much worse than existing methods. Hence, it would require

a lot of optimization before it could outperform the analytical superposition method.

But I wanted to learn more about the field and application of fundamental mechanics, improve my Python coding and discover the realms of academic research. Although I had decided to skip a publication, I did achieve all those goals in the end, so I guess we can conclude that all's well that ends well. A special thanks to my supervisors Can and Alejandro, to Jian for his assistance in Hybrida, to my family and to God above all.

Robbert-Jan Bosch